Gondwana Research 124 (2023) 39–60

Contents lists available at ScienceDirect

Gondwana Research

journal homepage: www.elsevier.com/locate/gr

Strong positive fractionation of chromium isotopes in iron formation of the Jacadigo Group (Brazil) – A link to enhanced atmospheric oxygenation during the Late Neoproterozoic

Trygvi Bech Árting [a], Paulo César Boggiani [b], Claudio Gaucher [c], Henrique Albuquerque Fernandes [b], Robert Frei [a,*]

[a] University of Copenhagen, Department of Geosciences and Natural Resource Management, Øster Voldgade 10, 1350 Copenhagen K, Denmark
[b] Instituto de Geociências, Universidade de São Paulo, São Paulo, SP, Brazil
[c] Instituto de Ciencias Geológicas, Facultad de Ciencias, Universidad de la República, Iguá 4225, 11400 Montevideo, Uruguay

ARTICLE INFO

Article history:
Received 17 March 2023
Revised 7 June 2023
Accepted 7 June 2023
Available online 1 July 2023
Handling editor: Franco Pirajno

Keywords:
Banda Alta Formation
Urucum iron formation Brazil
Chromium isotopes
Late Neoproterozoic
Marinoan glaciation

ABSTRACT

Cr isotopes recorded in iron formations (IF) are considered to have the potential to reflect the isotope signatures in respective ambient surface seawater. The ~600 Ma Fe and Mn deposits pertaining to the Banda Alta Formation (Urucum district, Mato Grosso do Sul, Brazil), comprise the world's youngest and largest Neoproterozoic sedimentary Fe and Mn formations (MnF). Shale normalized Rare Earth Element and Yttrium (REY) patterns of drillcore samples show flat, positively sloped patterns with absent Europium anomalies and near- to supra-chondritic Yttrium-Holmium ratios with negative Cerium anomalies, which imply intermittent mixing of freshwater with seawater. Redox sensitive element enrichment factors (Mo_{EF}, U_{EF}, Cr_{EF}) show positive correlation, indicating varying redox conditions across the Jacadigo Basin, with ephemeral euxinic conditions. The Cr isotope signatures across the Urucum IF ($\delta^{53}Cr_{auth}$ at: Morraria Grande + 0.93 ± 0.34 ‰, 2σ, n = 28; Morro do Rabichão + 0.5 ± 0.4 ‰, 2σ, n = 3; and Morro do Urucum ca. + 0.64 ‰, n = 1) are statistically indistinguishable from previously published surface outcrop samples at Morro do Urucum. Our new data support: (1) a stable supply of oxidized Cr potentially from continental sources at the time of deposition, implying high atmospheric O_2 levels in the Late Neoproterozoic; (2) insignificant alteration of the authigenic Cr isotope signals by tropical weathering despite surface iron up-concentration and leaching of carbonates, and (3) lack of isotope effects that would be associated with non-quantitative reduction processes and accompanying particulate transport to the chemical sediments in the Jacadigo Basin. The combined information from (isotope)geochemical data presented herein speak for a deposition of the Urucum IFs in restricted, periodically ice-covered and stratified sub-basins with partial connection to the open ocean, and for the presence of a sufficiently oxidative atmosphere which promoted a continuous supply of the surface waters with isotopically heavy Cr from the weathering landmasses at this time.

1. Introduction

Most Banded Iron Formations (BIF) were formed during the Archean Eon and Paleoproterozoic Era, with most widespread occurrence at ca. 2.5 Ga coinciding with the Great Oxidation Event (GOE) followed by global non-deposition of IFs during the late Paleoproterozoic and Mesoproterozoic (1.85–1.0 Ga) ((Eriksson et al., 2004) and references therein). The absence of BIF deposition in this period has been explained by complete lack or only weak ocean oxidation (e.g. (Bekker et al., 2010; Holland, 1984; Slack et al., 2007), or by widespread development of euxinic (anoxic and sulfidic) deep-ocean conditions along productive continental margins (Poulton et al., 2010). These environmental conditions in the late Paleoproterozoic and Mesoproterozoic were most likely associated with long pauses in global plate tectonic activity and plumes break out (e.g., (Stern, 2020)). After a billion years of scarce BIF deposition, widespread occurrence of Iron Formations (IF) appeared again in the Neoproterozoic. The Neoproterozoic IF were formed during times of substantial environmental changes, and many of them are interpreted as being deposited in association with proposed global glaciation events, such as during the Sturtian

* Corresponding author.
E-mail address: robertf@ign.ku.dk (R. Frei).

https://doi.org/10.1016/j.gr.2023.06.017
1342-937X/

(middle Cryogenian), Marinoan (late Cryogenian) and the Gaskiers (Ediacaran) glacial events (Halverson et al., 2010). During these time periods, stratified water column redox conditions developed, allowing the accumulation of large amounts of dissolved iron in the basins where iron formations were formed (Baldwin et al., 2012). Some major Neoproterozoic IFs are: the Shilu Group BIF of Tonian age (960–830 Ma: (Xu et al., 2014; Yu et al., 2022), the Rapitan Group in northern Canada, 715 Ma (Baldwin et al., 2012; Halverson et al., 2011; Klein and Beukes, 1993; Young, 1976); the Chuos Formation in Namibia, 750–650 Ma (Breitkopf, 1988; Lechte et al., 2018); the Braemar Ironstone in South Australia, 750–700 Ma (Lottermoser and Ashley, 2000); the Ediacaran Arroyo del Soldado Group (Frei et al., 2013; Gaucher et al., 2015), and the Jacadigo Group of the Urucum-Mutun ore district in Brazil/Bolivia, 580–695 Ma (Angerer et al., 2016; Baldwin et al., 2012; Frei et al., 2017; Freitas et al., 2011; Klein and Beukes, 1993; Klein and Ladeira, 2004; Macdonald et al., 2010; Morais et al., 2017; Viehmann et al., 2016). Some Neoproterozoic BIFs are unrelated to glacial processes (also often referred to as Rapitan type), and have been classified as Algoma type (e.g., (Basta et al., 2011; Sial et al., 2015; Stern et al., 2013)) or Superior type (e.g. (Gaucher et al., 2015; Yu et al., 2022).

In the aftermath of near-global glaciations, phytoplankton productivity increased (Planavsky et al., 2010), leading to increased O_2 in the atmosphere, and eventually to the Neoproterozoic oxidation event (NOE)(Frei et al., 2009). This was succeeded by the appearance of the Ediacara fauna at ~575 Ma (e.g., (Droser and Gehling, 2015; Narbonne, 2005). It has been suggested that deep ocean anoxia and ferruginous conditions were able to prevail throughout the latest Neoproterozoic and into the Cambrian (Canfield et al., 2008; Johnston et al., 2010; Li et al., 2010).

The Fe and Mn deposits in the Urucum district pertain to the Banda Alta Formation (Fig. 1) in Mato Grosso do Sul State, Brazil, and are associated with glaciogenic deposits. The Urucum IF is one of the world's youngest and largest Cryogenian sedimentary IF and Mn formation (MnF). This youngest Precambrian iron formation has been proposed to have been deposited during a near-global ice cover ("Snowball Earth" (Kirschvink, 1992)), preventing exchange of oxygen between atmosphere and oceans, and thereby causing accumulation of Fe(II) dissolved in the oceans. Among many debated models for the recovery from large-scale glaciation (e.g. (Allen and Etienne, 2008; Le Hir et al., 2009; Peltier et al., 2007), one model suggests that voluminous volcanic outgassing could have raised the atmospheric CO_2 to levels 350 times present atmospheric levels (PAL) and so could have caused extreme greenhouse conditions (Hoffman et al., 1998). This model was tested by (Frei et al., 2017) using the Cr isotope redox-proxy at Morro do Urucum (M. Urucum), and relying on the circumstance that the release mechanism of Cr from the continents has a major control on the Cr mass budget and significantly imparts on isotope composition of Cr in at least today's ocean's surface waters (Frei et al., 2014), besides of a substantial and potentially primary control by biological productivity in the photic water layers (Janssen et al., 2020; Scheiderich et al., 2015). In their study of Cr isotopes in the Urucum IF, (Frei et al., 2017) postulated that positively fractionated signatures must have been caused by widespread oxidative release of Cr(VI) from the continents, rather than by acidic release of Cr(III) caused by elevated CO_2 greenhouse-like concentrations.

Effects of surface run-off on the preservation of originally authigenic Cr (Cr_{auth}) isotope signals in IF outcrops has been advocated in a recent study on the 2.95 Ga Izermijn IF, South Africa, in which it was concluded that isotopically positively fractionated Cr in these IF resulted from interaction of run-off surface water and secondary reductive assimilation of positively fractionated Cr(VI) into iron oxides (Albut et al., 2018; Albut et al., 2019). These authors postulated that such modern process can mimic a positive signal that is derived from modern oxidative weathering, rather than representing an original authigenic signal that could have potentially prevailed during the time of deposition of the IF (Albut et al., 2018; Albut et al., 2019). In this study we expand the work published by (Frei et al., 2017) on a surface stratigraphic profile of M. Urucum, by including drillcore samples from the Santa Cruz deposit on neighboring Morraria Grande (M. Grande; Fig. 1), and also encompass eight drillcore samples collected by (Viehmann et al., 2016) at M. Urucum and Morro do Rabichão (M. Rabichão; Fig. 1), with the aim to reconcile recent findings in the Izermijn IF (Albut et al., 2018; Albut et al., 2019). We present Cr stable isotopes, rare earth element and yttrium (REY) patterns, and redox sensitive trace element and major element data, in order to evaluate the effects of modern weathering on the Cr isotope signal in the Urucum IF, and to provide a basin wide model for the Cr-isotope signals.

2. Cr sources and pathways

Contribution of Cr to the oceans comes from either run-off from the continents or through hydrothermal vent fluids. While the latter contributes with isotopically unfractionated Cr ($\delta^{53}Cr = -0.12 \pm 0.11$ ‰; (Schoenberg et al., 2008), continentally derived Cr may be positively fractionated as a result of oxidative weathering release. Under oxidative weathering conditions, oxygen in the atmosphere is a driver for the oxidation of immobile Cr(III) to soluble Cr(VI) in the presence of Mn-oxides, which function as reaction catalysts (Oze et al., 2007). Partial reduction of the mobilized Cr(VI) leads to positively fractionated Cr isotopes in the mobile fraction (D'Arcy et al., 2016; Farkaš et al., 2013; Frei et al., 2009; He et al., 2020; Novak et al., 2017; Paulukat et al., 2015; Wu et al., 2017). The positively fractionated dissolved Cr (VI) compounds are transported from the continents to the oceans where they either are sorbed onto particles or are, either biologically (e.g., (Janssen et al., 2020; Scheiderich et al., 2015) or abiologically (Frei et al., 2009; Janssen et al., 2022), reduced to insoluble Cr (III) bearing species and deposited in marine sediments. The Cr input budget of ocean waters is therefore determined by a mixture between three end members: (1) hydrothermal Cr(III), (2) unfractionated continental Cr(III) carried by suspended load or dissolved organically bound compounds and (3) soluble and fractionated continental Cr(VI). In the modern ocean, the initial Cr isotope signal may be altered by biogenic redox processes in the water column, for example by organic matter reduction (Janssen et al., 2020; Rickli et al., 2019), by incorporation into carbonates (Frei et al., 2011; Wei et al., 2018a), and by in-vitro effects of $CaCO_3$ precipitating organisms such as bivalves (Bruggmann et al., 2019a; Frei et al., 2018) and planktonic foraminifera (Wang et al., 2016a). If dissolved Cr occurs predominantly as Cr(VI), and if there is surplus fertilization of the ocean waters with dissolved ferrous [Fe(II)] iron, chemical sediments such as IFs are capable of recording the positively fractionated seawater $\delta^{53}Cr$ signature, if reductive stripping of Cr through the Fe-oxy(hydr)oxide shuttle is efficient and quantitative (Døssing et al., 2011; Frei et al., 2009). In such a scenario, there is an ultimate link of the fate of Cr between atmospheric oxygenation, intensity of release of chromium from the continents, levels of primary productivity, and Cr records in iron-rich chemical sediments. The Cr isotope signals captured in IFs have in the past been used to infer on the evolution of Earth's atmospheric oxygenation through time, and ultimately as a record of climate changes in the Precambrian period (Frei et al., 2016; Frei et al., 2009; Konhauser et al., 2011; Wei et al., 2018b).

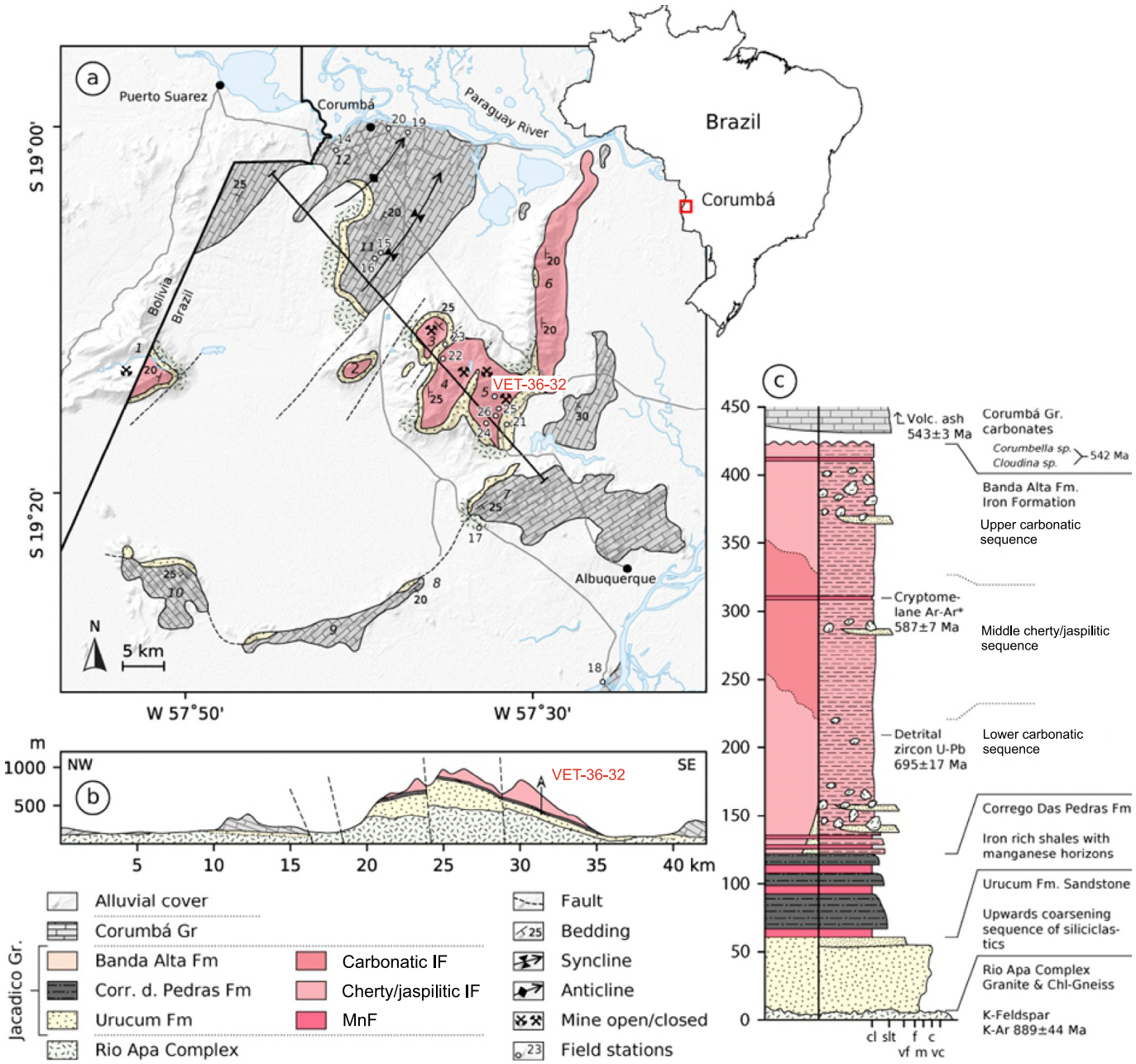

Fig. 1. Local geology of the Corumbá area: (a) Simplified geological map around Corumbá. Locations: 1, Morro do Jacadigo (Mutum); 2, M. da Tromba dos Macacos; 3, M. do Urucum; 4, M. Santa Cruz; 5, M. Grande; 6, M. do Rabichão; 7, M. do Zanetti; 8, M. Pelada; 9, M. d'Aguassu; 10, M. do Sajutá; 11, Laginia Quarry; 12, Corcal Quarry (Modified after (Angerer et al., 2016). Location of drill hole VET-36-32, from which samples have been analyzed herein, is indicated (b) Simplified NE-SW striking profile, marked with barred line on (a); location of drill hole VET-36-32 is indicated. (c) Summarized stratigraphic profile, showing known radiometric ages published by (Babinski et al., 2013; Frei et al., 2017; Piacentini et al., 2013). Details see text. cl = clay, slt = silt, vf = very fine, f = fine, m = medium, c = coarse, vc = very coarse.

3. Geological setting

The geology of the Corumbá region (Fig. 1) has been described in previous publications (Freitas et al., 2011; Piacentini et al., 2007; Piacentini et al., 2013; Trompette et al., 1998), and more recently the tectonic, stratigraphic, structural and textural relations were summarized by (Viehmann et al., 2016), (Angerer et al., 2016), (Freitas et al., 2011) and more recently, by (Polgári et al., 2021) and (Hiatt et al., 2020). Likewise, we refer to detailed mineralogical and sedimentary descriptions of the Urucum IF contained in the articles by the aforementioned authors.

The Neoproterozoic rocks in the Urucum district are part of the Jacadigo Group and pertain to the Río Apa Block of the southernmost part of the Amazonian Craton. Sediments were deposited in a rift to shelf setting (Trompette et al., 1998). Rocks of the Jacadigo Group are unconformably overlain by Ediacaran limestones and dolostones of the Corumbá Group (e.g., (Almeida, 1965; Gaucher et al., 2003; Hiatt et al., 2020; Morais et al., 2021; Walde et al., 2015). The Jacadigo Group continues into Bolivia where it is known as the Boquí Group.

The basement of the Rio Apa Block, which mainly consists of granite and chlorite rich gneisses (Angerer et al., 2016; Viehmann et al., 2016) is unconformably overlain by the Jacadigo Group which is divided into three formations (Fig. 1): (1) The Urucum Formation, comprising fine to medium-coarse grained siliciclastics with local cross bedding and inverse grading (Fig. 2;. (Freitas et al.,

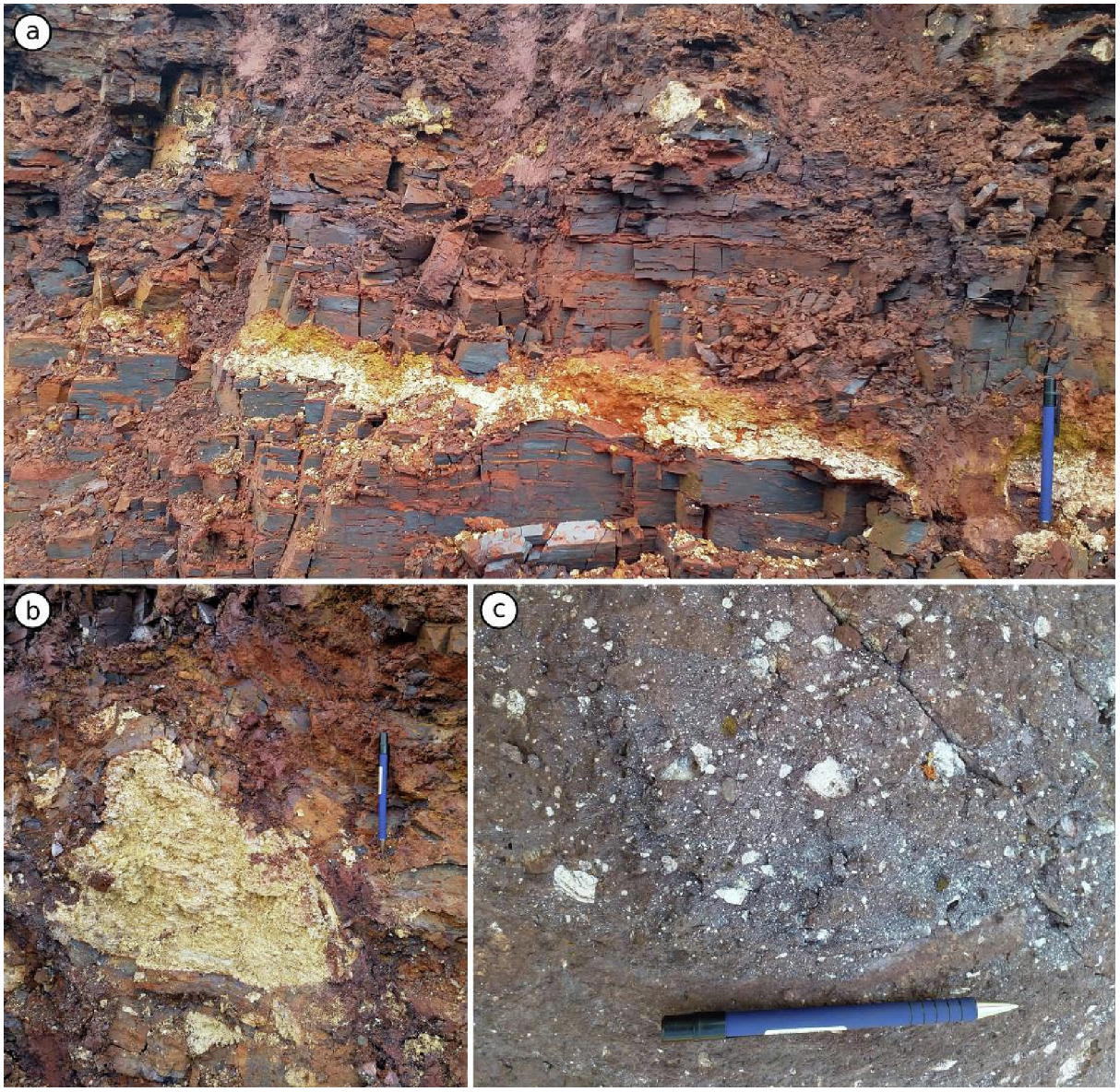

Fig. 2. Field images: (a) Density flow deposit near the base of Banda Alta Formation, Vale Corumbaense mine. Sharp erosional base overlain by depression filling kaolinite which grades into a Fe-oxide matrix supported conglomerate with kaolinized pebbles and boulders; (b) Kaolinized granitic boulder in the deposit shown in (a) Notice disseminated smaller pebbles surrounding the boulder; (c) Density flow deposit in the middle of Banda Alta Formation, Vectorial mine, M. Grande, with up to 4 cm wide basement clasts hosted in Fe-oxide matrix.

2011) and (Angerer et al., 2016) interpret these as fluvial deposits; (2) The Córrego Das Pedras Formation, comprising sandstone, arkose and micro-conglomerate, as well as up to three primary Mn-oxide layers (dominated by cryptomelane and braunite, <2m thickness) (Freitas et al., 2011; Urban et al., 1992; 3) The Banda Alta Formation, comprising a 360 m-thick succession of IF (Fig. 1), is composed of three distinct layers: a basal and upper carbonatic sequence, and an intermediate cherty sequence. (Angerer et al., 2016) and (Dorr, 1945) refer to this as the Santa Cruz Formation, and do not distinguish the transitional Córrego das Pedras Formation as a different stratigraphic unit. The IF comprises alternating 0.5–10 cm, laterally continuous hematite-chert bands. Manganese oxide dominated layers (42–48 % Mn) occur in four separate horizons up to 3 m thick, and occur as tabular beds, near the base of the Banda Alta Formation, while thinner beds appear near the top. Diamictite layers are discontinuously intercalated with the IF, with a lower diamictite sequence occurring at the base with waning frequency throughout the first 100 m, a second 30 m-thick diamictite in the middle of the formation, and a third 60 m-thick sequence at the top (Fig. 2). The Jacadigo Group contains no significant tectonic repetitions (Angerer et al., 2016).

The depositional age of the Banda Alta Formation is indirectly constrained: An upper age limit of 695 ± 17 Ma is defined by detrital zircon U-Pb ages from shaley beds in the IF (Frei et al., 2017), recently confirmed by a 690 ± 18 Ma U-Pb age reported by (Freitas et al., 2021). A lower age limit has been determined by U-Pb zircon ages of 543 ± 3 Ma (Babinski et al., 2013), and 555 ± 0.3 Ma (Parry et al., 2017) from ash layers in the overlying Corumbá Group, consistent with the Ediacaran fossil assemblage in these rocks (e.g. *Cloudina* sp. and *Corumbella* sp.; (Gaucher et al., 2003; Morais et al., 2021; Walde et al., 2015), as well as by a 585–582 Ma Ar*-Ar age for Mn-bearing minerals in the Jacadigo Group, interpreted as representing an early diagenetic event (Piacentini et al., 2013). This makes the Banda Alta Formation con-

temporaneous with the Gaskiers glaciation (Alvarenga et al., 2011; Gaucher et al., 2009). The younger Gaskiers age preferred by (Frei et al., 2017) is based on the occurrence of the Ediacaran fossils immediately above the IF, as well as based on a correlation of the Banda Alta Formation with iron rich shales of the Puga Formation (part of the northern Paraguay Belt within the Serra da Bodequena (Alvarenga et al., 2011; Frei et al., 2017; Trompette et al., 1998), which is exposed ca. 50 km to the SSE of Corumbá (outside map area of Fig. 1). The Puga Formation sediments are correlated with Ediacaran glacial deposits in Uruguay dated by U-Pb on zircon between 590 and 573 Ma (Oyantcabal et al., 2009; Will et al., 2021). In addition, a tentative five point Sm-Nd isochron on pure IF samples of the Banda Alta Formation yielding 566 ± 110 Ma (Viehmann et al., 2016), although less precisely defined, is in support of the Gaskiers age of the Banda Alta Formation IF. However, a Marinoan age around 635 Ma cannot be ruled out with the available geochronological evidence.

The primary evidence for *syn*-sedimentary glacial processes in the Banda Alta Formation are outsized granitic clasts hosted within the IF and MnF, a few centimeter to up to 10 m in their largest maximum dimension, with elongated clasts often showing long axes perpendicular to bedding (“bullet clasts”, (Gaucher et al., 2015).. These have been suggested to be glacial in origin (i.e., representing dropstones; (Trompette et al., 1998; Urban et al., 1992). However, others (e.g., (Freitas et al., 2011) suggested a non-glacial origin for these lonestones and explained their occurrence by transport with sediment gravity flows and slumping of oversteepened topography, as is evidenced by the presence of gravity flows with smaller arkose and feldspathic sandstone clasts and occasional outsized granitic clasts (Trompette et al., 1998), compatible with IF breccia and gravity flow shown in (Fig. 2). However, gravity flows (e.g. grain and mud flows) are also very common in glaciomarine settings, often in association with rain-out debris (Einsele, 2000). The deformation around granitic boulders is generally more pronounced above them which can be explained by differential compaction of less competent chemical deposits around rigid granitic clasts. On the other hand, dolostone layers in the Banda Alta Formation have negative $\delta\ ^{13}C$ values (-7.0 to −3.4 ‰; (Angerer et al., 2016; Klein and Ladeira, 2004), which are more compatible with signals of carbonates deposited during or after glaciation events (Halverson et al., 2005). Furthermore, (Freitas et al., 2021) recently conceded a glacial origin for the Jacadigo IF, and interpreted unconformities as the effect of glacioeustatic uplift. Thus, the IFs were classified as a Rapitan-type (Frei et al., 2017; Gaucher et al., 2015; Klein and Beukes, 1993).

4. Materials and methods

4.1. Samples

Samples were obtained from Vectorial Ltd. borehole STCR-DD-36–32 (W57°31′58.30″ S19°14′59.98″) at the Santa Cruz deposit, Morraria Grande (M. Grande) (Fig. 1), which was sampled at 10-meter intervals in iron rich intervals, avoiding any occurrence of arkose/feldspathic sandstone. Hematite bands (referred to as mesobands herein) were separated from these samples with a diamond bladed rock saw and powdered in an agate mill. These samples are labeled VET, and are incrementally numbered with sampling depth, and referred to as IF samples. Although care was taken to select hematite mesobands, some samples show carbonate phase leaching (VET-2, 4, 5, 13 and 14; Fig. 3), in some drillcore samples it was impossible to obtain a pure hematite mesoband sample, i.e., VET-20 (Fig. 3). Bulk drill core geochemical results used herein are those from core logging provided by the Vectorial Ltd. mining company. Eight powder aliquots of samples described by (Viehmann et al., 2016) were obtained for Cr isotope analysis. These comprise three pure IF samples from Morro do Rabichão (M. Rabichão, UR-62-*, Fig. 1) and five samples from Morro do Urucum (M. Urucum, UR-51-*, Fig. 1), whereby two of those are Mn IFs from the Corrego Das Pedras Formation (CD Pedras Formation) directly underlying the Banda Alta Formation (Fig. 1). Representative drillcore samples are shown in Fig. 3.

4.2. Chemical analyses

Trace element concentrations were determined using solution ICP-MS (Inductively Coupled Plasma Mass Spectrometry). The samples were dissolved in a mixture of concentrated HCl-HNO_3-HF. The solutions were evaporated to incipient dryness and re-dissolved twice in concentrated HCl, and once in concentrated HNO_3. Finally, the samples were re-dissolved in 0.5 M HNO_3 + 0.01-M HF and analyzed with a Bruker Aurora Elite ICP-MS at the University of Copenhagen using artificial standards for calibration and ^{115}In and ^{187}Re as internal standards to monitor drift and matrix effects. An iron formation standard (GIT-IWG IF-G; (Govindaraju, 1984)) was analyzed as an internal control sample. Major elements were analyzed at Bureau Veritas Canada Ltd. with method LF300. Major element concentrations of bulk core intervals from core STCR-DD-36–32 were obtained from Vectorial Ltd (Table S1).

4.3. Chromium isotope analyses

Powdered samples were combined with a $^{50-54}Cr$ double spike, digested in a 1:3:1 solution of concentrated HCl, HNO_3 and HF, and passed over 3 gravity driven columns: (1) Fe-removal by 6 N HCl extraction by passing the sample solution twice over a PolyPrep column packed with 2 mL 100–200 mesh BioRad DOWEX AGx8 anion exchange resin following (Frei et al., 2009; 2) A pass over the same column and resin as step 1, following the method of (Schoenberg et al., 2008) to remove other matrix elements; (3) A purification over BioRad columns packed with 2 mL DOWEX 200–400 mesh AG50Wx8 cation resin preconditioned with 0.5 M HCl following the procedure of (Trinquier et al., 2008). The samples were dissolved and collected in Savillex Teflon beakers between all steps. The acids were in-house distilled Merck Emsure 37 % HCl and 65 % HNO_3 acids, diluted as needed with Milli-Q ultrapure water. Subsequently, the samples were loaded on Re-filaments with 1.5 μL silica gel and 0.5 μL 1 M H_2PO_4 and 0.5 μL saturated H_3BO_3 (further details in (Døssing et al., 2011; Frei et al., 2016; Paulukat et al., 2015), and analyzed in static mode on an IsotopX/GV Isoprobe-T TIMS instrument. Isotopic compositions and Cr concentrations were reduced from raw data by using exponential mass fractionation laws combined with the Newton-Rhapson method implemented in an in-house Python 3 program (Rudge et al., 2009) and references therein). Chromium isotope ratios are reported using delta notation relative to National Institute of Standards, Standard Reference Material 979 (SRM979):

$$\delta^{53}Cr = \left(\frac{\left[{}^{53}Cr/{}^{52}Cr \right]_{sample}}{\left[{}^{53}Cr/{}^{52}Cr \right]_{SRM979}} - 1 \right) \cdot 1000‰$$

Spiked SRM979 was analyzed routinely, at similar beam intensity (^{52}Cr at 500 and 1000 mV) and analysis time as the samples, for assuring long term stability. Amplifier gain calibration was run at least two times a day during analysis runs. As the spike is calibrated to NIST SRM 3112a, raw analyzes were offset by the mean measured value of spiked SRM979. The spiked SRM979 analyzes yielded a 2σ external reproducibility of ±0.09 ‰ for 500 and

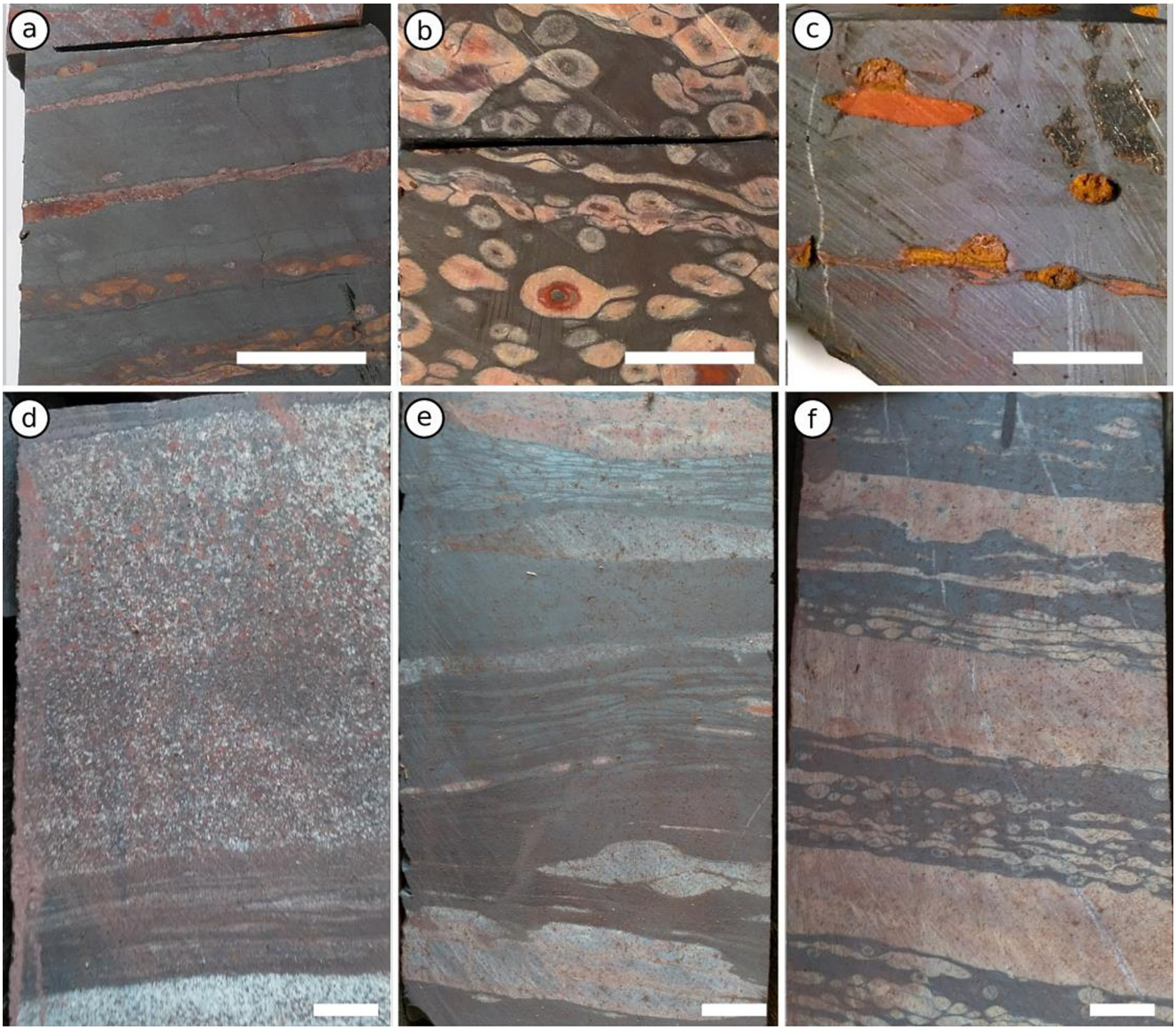

Fig. 3. Samples and representative images from the studied drill-core: (a) Sample VET-27: banded IF with nodular and granular bands (281.30 m; b) Sample VET-20: nodular IF with carbonaceous ooids (212.00 m; c) Sample VET-05: IF with leached carbonates (38.30 m; d) Inversely graded granular layer in the basal part of Banda Alta Formation (325 m, 4.6 m below sample VET-31; e) Deformed carbonatic and iron-rich nodules (311.8 m, above sample VET-30; f) Banded and nodular IF section (273 m, 2 m below sample VET-26).White bars are 1 cm wide.

1000 mV ^{52}Cr signals. In addition, five samples were processed and analyzed a minimum of 5 times at different intensities in order to determine sample and data collection reproducibility (Fig. 4).

5. Results

5.1. Major elements

Own data of IF mesobands are listed in Table S1, whereas bulk core samples provided by Vectorial Ltd. are listed in Table S2. Depth distribution of Fe, SiO_2, CaO + MgO and Al_2O_3 concentrations in the IF mesobands and in bulk core samples are plotted in Fig. 5 for an overview purpose.

At the base of the Banda Alta Formation, between c. 300–350 m depth, there is a gradual transition from the siliciclastics of the underlying Corrego das Pedras Formation, to carbonatic IF in the lower Banda Alta Formation. This is reflected by the gradual decrease in concentrations of SiO_2 and Al_2O_3 in the bulk core samples up until 320 m. There is an absence of pure hematite mesobands in this interval and we therefore did not sample them. This basal interval is succeeded by two IF intervals (Fig. 5): (1) the section between 350 and 150 m is characterized by carbonatic-cherty IF with bulk CaO + MgO of ca. 10 %, Al_2O_3 < 1 % wt., bulk SiO_2 around 20–30 % wt. and presence of carbonates (indicated by the jump towards higher CaO + MgO and lower Fe and SiO_2 concentrations below ~150 m particularly in the bulk core profile, but also reflected in the corresponding changes in the IF mesoband compositions (Fig. 5) (2) at 150 m there is a transition to cherty IF, with low CaO + MgO (<1 % wt.), a transition marked by the reappearance of gravity flow deposits, which are interspersed with pure IF beds throughout the upper half of the core. This is reflected by an increase in Al_2O_3 (up to 10 % wt.) and SiO_2 fluctuating between 30 and 50 % wt. (Fig. 5).

The IF samples from M. Grande (Table S1) mainly comprise hematite and chert mesobands, with Σ Fe_2O_3 (as total ranging between 70 and 97 % wt., except samples VET-20, −24 to 31 with

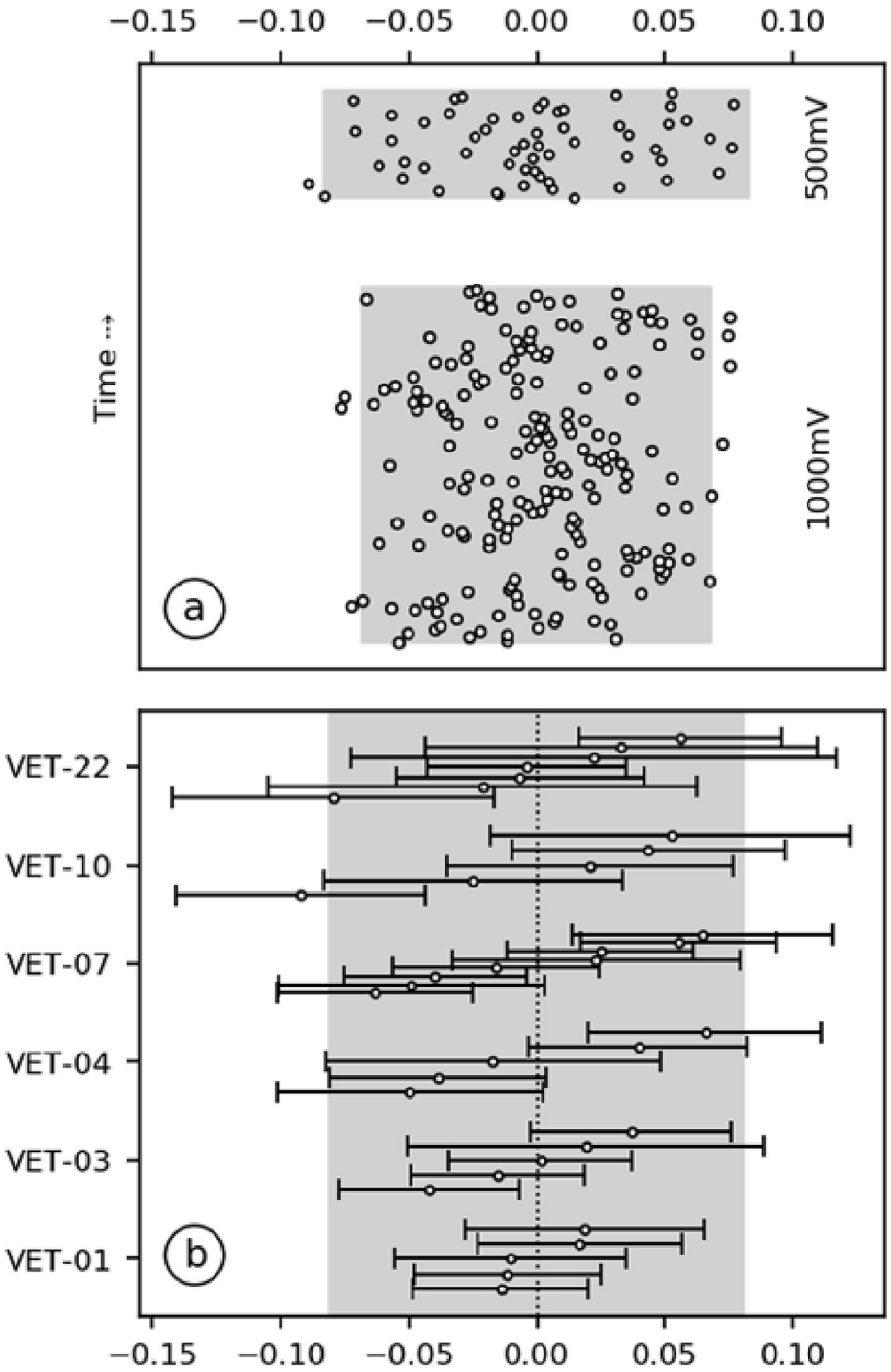

Fig. 4. Reproducibility of $\delta^{53}Cr_{SRM979}$ values of: (a) <individual analyses of SRM979 with 52Cr beam intensities of 500 mV and 1000 mV, respectively. Gray fields display 2 σ intervals; (b) Repeated analyses of 5 samples processed separately through chemistry. Cr isotope compositions are shown as deviation from the respective sample means, errors are 2SE internal errors, and the gray field shows 2 σ of the analyses of ±0.08 ‰.

Fe_2O_3 of 50–60 % wt. (Table S1; Fig. 5). Further, the SiO_2 concentrations form two apparent groups: One below ~10 % wt. and the other group in the range 15–50 % wt. (Fig. 6). The distinction between these groups is not evident stratigraphically, although high SiO_2 samples are more common in the upper siliceous interval (Fig. 5). CaO and MgO in the IF samples are generally low (≪1 % wt.), but respective concentrations in the lower carbonaceous interval samples may reach up to 11 % wt. CaO + MgO (Table S1; Fig. 5). The elevated Al_2O_2 observed in bulk samples (Table S1) is not reflected in the IF mesoband samples, where values are in the range of only 0.03–0.32 % wt. (Table S1; Fig. 5).

The bulk Al_2O_2 shows weak correlation with bulk SiO_2, although this correlation breaks down in siliciclastic intercalations where the Al_2O_3/SiO_2 is significantly higher. The Al_2O_3 in the hematite mesoband separates is however at a constant low concentration, attesting to only small contamination by detrital silicate components (Table S1, Fig. 6).

These variations reflect the mixing in a four-component system with a primary variation between non-aluminous SiO_2 phases (i.e.

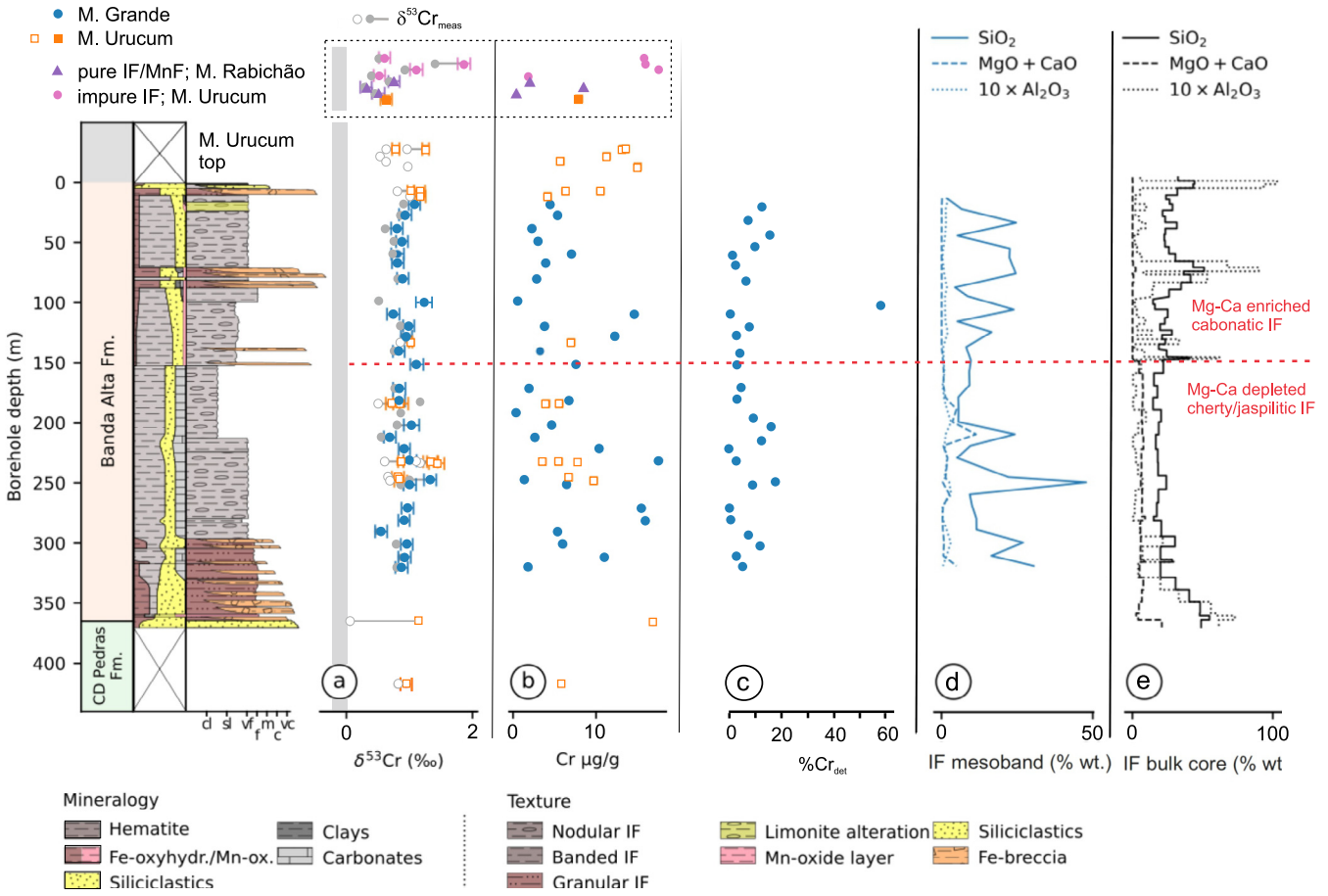

Fig. 5. Lithological log of Vectorial drillcore VET-36-32 indicates layers with detrital (siliciclastic) input, mobilization of IF (Fe-breccia) and (limonite) alteration. Geochemical variations: Filled symbols are new data from this study, open symbols from surface outcrop samples at M. Urucum (Frei et al., 2017). (a) $\delta^{53}Cr_{auth}$ (blue circles from the VET-36-32 core studied herein; orange squares from (Frei et al., 2017) at approximate stratigraphic levels; filled orange square from a drillcore sample of (Viehmann et al., 2016) at M. Urucum; purple triangles and pink circles mark pure and impure IF/MnF drillcore samples, respectively, from M. Rabichão and M. Urucum (Viehmann et al., 2016) analyzed herein; grey circles are $\delta^{53}Cr_{meas}$). Light shaded field depicts Cr isotope compositions of igneous silicate Earth reservoirs (Schoenberg et al., 2008; b) Cr concentrations; (c) Proportion of detrital Cr relative to total Cr in hematite mesobands, expressed in % (d) Hematitic mesoband compositions with regard to SiO_2, MgO + CaO and Al_2O_3; (e) Core bulk compositions provided by Vectorial Mine Ltd. Samples without stratigraphic relation are plotted in the insert above the stratigraphic profile, encased in a dashed line rectangle. cl = clay, slt = silt, vf = very fine, f = fine, m = medium, c = coarse, vc = very coarse. (For interpretation of the references to colour in this figure legend, the reader is referred to the web version of this article.)

jasper) and Fe_2O_3 bearing iron oxides, mixed in with independent Al-silicates (clay, high Al_2O_3) and carbonate components (high MgO and CaO; Figs. 6, 7).

5.2. Rare earth elements and yttrium

Trace element concentrations of mesoband samples are also listed in Table S1. Shale normalized REY anomalies were calculated following the recommendations of (Bolhar et al., 2004) and (Bau and Dulski, 1996) using the geometric mean to estimate the unfractionated reference concentration and normalized to Post-Archean Australian Shale (PAAS, (McLennan, 1989; Taylor and McLennan, 1985):

$$Eu/Eu^{*} = Eu_N \cdot Sm_N^{-2/3} \cdot Tb_N^{-1/3}$$

$$Ce/Ce^{*} = Ce_N \cdot Pr_N^{-2} \cdot Nd_N$$

Relative abundance of Y in marine sediments is determined as the Y-Ho ratio, with deviation from the chondritic value (ca. 28; (McDonough and Sun, 1995) being indicative of a faster scavenging of Ho relative to Y in seawater by different complexation with respect to seawater inorganic ligands (mainly carbonate ions) and soft organic ligands (though unspecified) of the surface of particulate matter (Nozaki et al., 1997). Fractionation of Y and Ho during weathering and fluvial transport to the ocean appears to have minor influence on the relative abundance of Y and Ho in seawater (Bau, 1999). $\sum$ REE for the iron separates from M. Grande studied herein is in the range 11 µg/g–92 µg/g, with a mean of 43 µg/g. Shale normalized REY patterns are LREE depleted (Pr/Yb_{PAAS} 0.2–1.1), exhibit negative Ce*/Ce (0.5–0.9) and are characterized by circumneutral Eu*/Eu (0.97–1.11), with a single positively fractionated sample (Eu*/Eu = 1.77) (Table S1; Fig. 8a). Y-Ho ratios vary between 22 and 40, with most samples having a neutral to positive ratio (≥28), except for 3 samples from M. Grande (Table S1; Fig. 8a).

5.3. Redox sensitive trace elements

The redox sensitive elements Cr, Mo and U enter the oceans in their oxidized states Cr(VI), Mo(VI) and U(VI) after release and transport from the continents (Algeo and Maynard, 2008; Frei et al., 2014; Partin et al., 2013). Under ferruginous conditions, reduction of Cr(VI) to Cr(III) by upwelling Fe(II) is efficient and complete, and the low solubility product is incorporated into colloidal iron formation precursor phases (ferric oxy-(hydr)oxides,

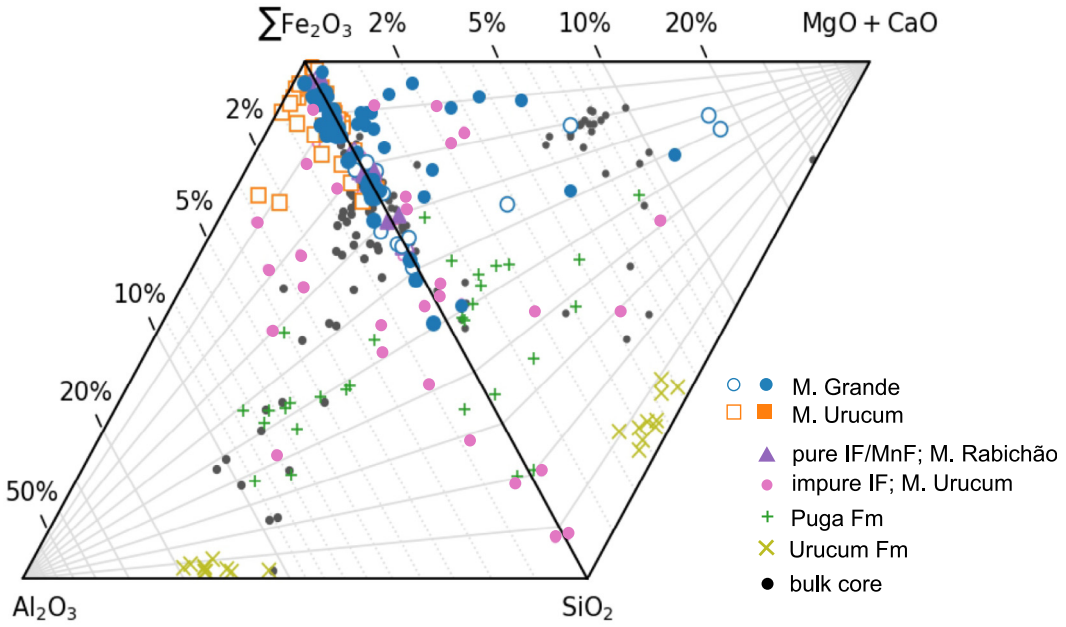

Fig. 6. Bi-ternary diagram showing major element variations, with ΣFe_2O_3 and SiO_2 across the diagonal representing relative amount of Fe-oxide and jasper. The two end members Al_2O_3 and MgO + CaO represent detrital and carbonate impurities, respectively. Diverging gridlines show constant Fe-Si ratios at 10 % intervals and scaled 1 and 10 % intervals towards the Al_2O_3 and CaO + MgO endmembers. Filled symbols are from this study, except dark gray filled circles which depict bulk core samples provided by Vectorial Mine Ltd.). Open symbols and crosses indicate data from (Angerer et al., 2016), (Viehmann et al., 2016) and (Frei et al., 2017).

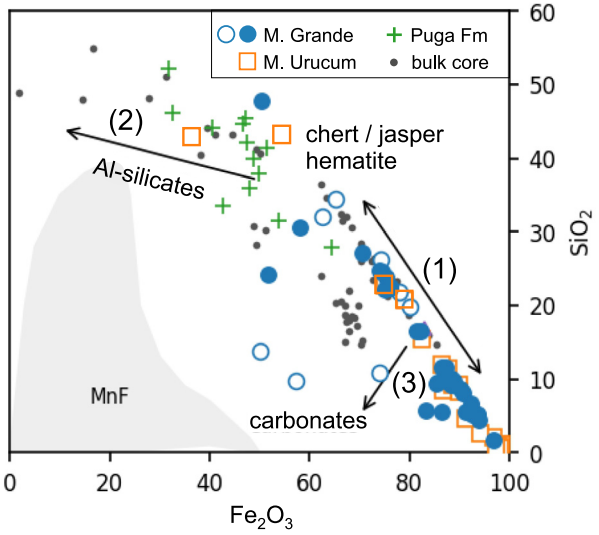

Fig. 7. Fe_2O_3 vs. SiO_2 variation diagram showing: (1) Mixture between cherty/jaspilitic- and hematiticendmembers for IF mesoband samples; (2) Deviation trend for carbonatic IF; and (3) for Al-silicate detrital contamination. Symbols as in Fig. 6, where filled symbols (except dark gray filled circles which depict bulk core samples provided by Vectorial Mine Ltd.) indicate samples from this study, and open symbols and crosses indicate data from (Angerer et al., 2016), (Viehmann et al., 2016) and (Frei et al., 2017).

(Frei et al., 2009)). Like the oxidized species of Cr and U, Mo(VI) as molybdate (MoO_4^{2-}) is soluble, and under oxidizing conditions is slowly removed by incorporation into Mn-oxides. Under euxinic conditions, Mo forms the thiomolybdate ion, which is particle reactive and is sequestered by Fe-Mn oxides, Fe-sulfides, organic material and clay minerals (Algeo and Tribovillard, 2009). Similarly, U (VI) is adsorbed by ferric oxy-(hydr)oxides as an oxidized species, and through subsequent reduction to U(IV) it is incorporated in, e.g. goethite (e.g. (Hsi and Langmuir, 1985; Liger et al., 1999; Partin et al., 2013).

Concentrations of the redox sensitive trace elements Cr (0.41–17.59 μg/g), Mo (0.03–1.04 μg/g) and U (0.06–5.96 μg/g) are comparatively low in samples from M. Grande (Table S1). Given the mineralogy of the samples, Cr and U are likely to be associated with hematite in the iron rich mesobands.

Enrichment factors (EF) are calculated to estimate the relative enrichment of the respective redox sensitive trace elements in comparison to their continental sources:

$$Me_{EF} = \frac{[C_{redox}/C_{ref}]_{sample}}{[C_{redox}/C_{ref}]_{source}}$$

Me_{EF} is the metal enrichment factor, and C_{redox} and $C_{ref.}$ are the concentrations of the trace element of interest and a reference element, respectively. The reference element should be insoluble and abundant in detrital silicate phases, e.g., Al, Ti, Th and others. We use Al_2O_3 in this paper as Al is a major element in the detrital components. The source is assumed to be PAAS-like (18.9 % Al_2O_3, 110 μg/g Cr, 0.485 μg/g, Mo, 3.1 μg/g U; (Taylor and McLennan, 1985); Mo from (Marx and Kamber, 2010)).

The Cr, Mo and U EFs are plotted in Fig. 9 along with IF samples from the Santa Cruz deposit (on M. Grande) from (Angerer et al., 2016), and with so-referred "pure" (samples with negligible detrital contamination), and "impure" (samples with elevated detrital contamination and/or samples that have been altered during weathering) IF samples from M. Urucum and M. Rabichão published by (Viehmann et al., 2016). In addition, the surface outcrop samples from M. Urucum published by (Frei et al., 2017) are plotted in Fig. 9. For reference, iron rich shale and IF samples from Fazenda do São Manoel pertaining to the Puga Formation (Frei et al., 2017) are also included. The EFs are highly variable but mostly positive for all the three elements in the Urucum region, so also for the M. Grande samples studied herein (Fig. 9a, b). Over-

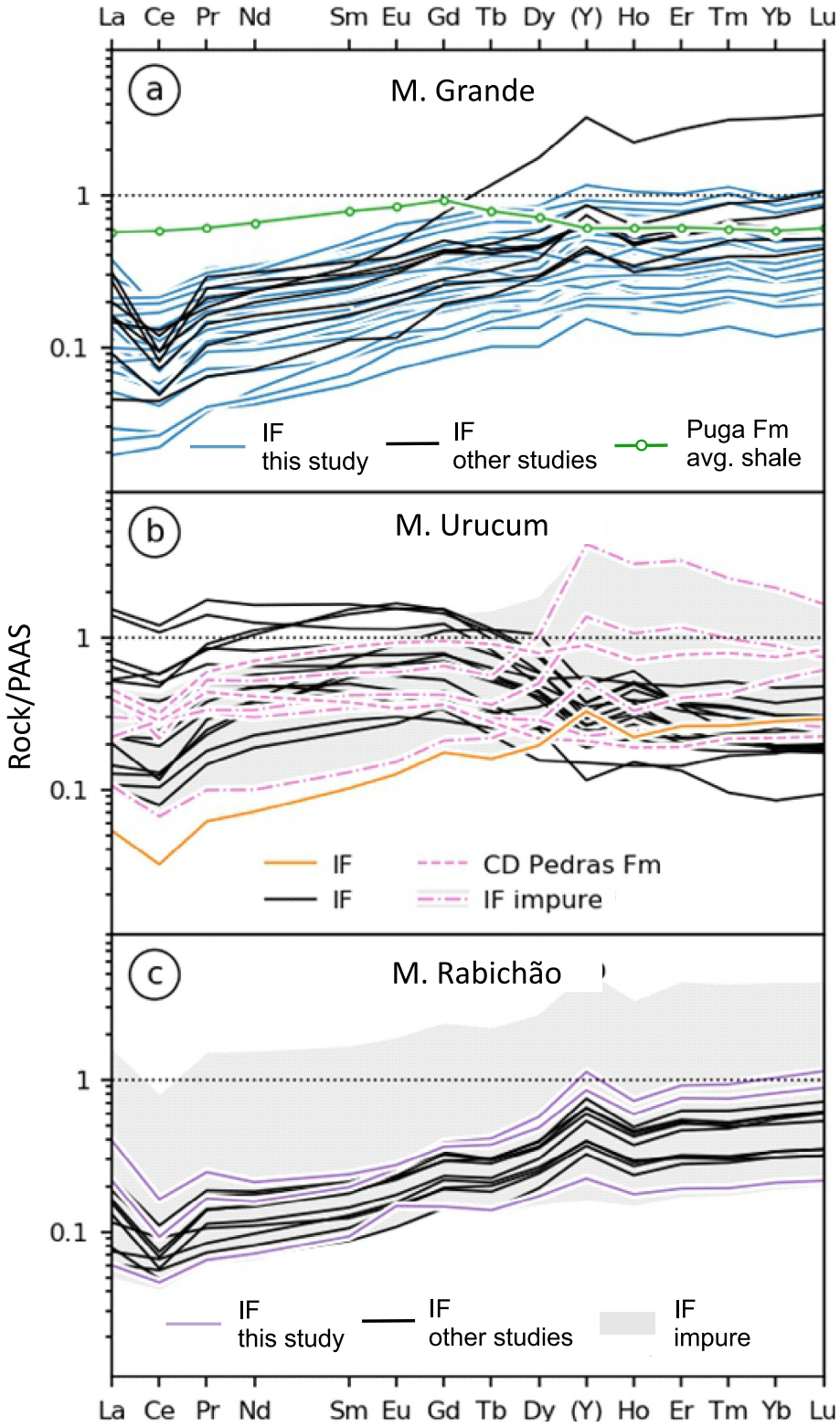

Fig. 8. Published and new shale normalized rare earth element patterns (PAAS; (Taylor and McLennan, 1985) of IFs from various "morros" of the Urucum mining district. (a) Hematite mesoband samples (blue lines) from M. Grande studied herein display seawater like, positively sloped to convex up REY patterns, with varying negative Ce anomalies, absent Eu anomalies, and neutral to positive Y/Ho. IF patterns in black are those classified into REE I and REE II patterns by (Angerer et al., 2016) from the Santa Cruz deposit on M. Grande. These are compatible with those studied herein. For comparison and reference, an average REY pattern of iron rich shales from the Puga Formation (Frei et al., 2017) is near horizontal and flat. (b) REY patterns of one pure (orange line), three impure (purple dash-dotted lines) IFs and two Mn IFs (purple dashed lines) from M. Urucum (Viehmann et al., 2016) that are compared with the surface IF samples (black lines) from the study of (Frei et al., 2017). The latter generally display strong LREE to MREE enrichments, while in contrast, the pure IF sample is characterized by a seawater-like REY pattern resembling those from M. Grande (displayed in (a)). Impure IF samples reported in the study of (Viehmann et al., 2016) are comprised in the gray shaded area for comparison. (c) M. Rabichão pure IF samples in black lines (Viehmann et al., 2016); 3 samples analyzed herein for Cr isotopes distinguished by purple lines) all show seawater-like patterns similar to the IFs from M. Grande. (For interpretation of the references to colour in this figure legend, the reader is referred to the web version of this article.)

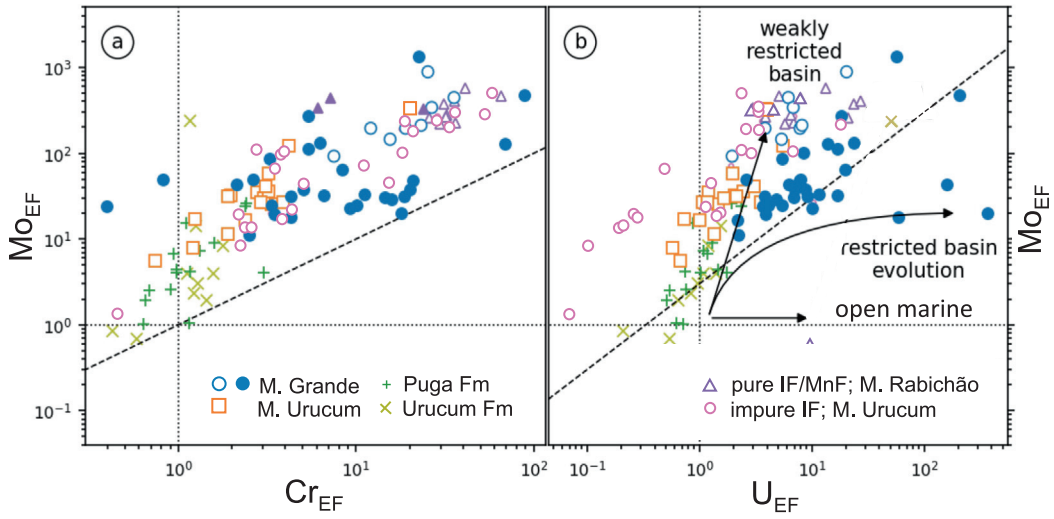

Fig. 9. Enrichment factors for redox sensitive elements. (a) Mo_{EF} against Cr_{EF}, showing positive correlation for IF and Mn IF drill-core samples and surface samples from this study (blue filled circles; purple filled triangles and small circles; orange filled square (b) Mo_{EF} against U_{EF} (diagram adapted from (Algeo and Tribovillard, 2009)) with arrows pointing to three types of modern redox-sensitive basins. Data arrays show weak linear correlation for surface samples (M. Urucum and Puga Formation iron rich shales; (Frei et al., 2017) and for drillcore IF samples from M. Urucum and M. Rabichão (Viehmann et al., 2016) and from M. Grande (Angerer et al., 2016); all open symbols). Drillcore mesoband IF samples (blue filled circles) studied herein exhibit enhanced scatter with significant deviation of at least three samples from the open marine – restricted basin trajectory towards elevated U_{EF} relative to Mo_{EF}, pointing to occasional restricted euxinic depositional basin conditions. Siliciclastic samples from the Urucum Formation (light green crosses) are from (Viehmann et al., 2016). Dashed line marks the covariant trend line for samples from the Black Sea in Fig. 4c of (Algeo and Tribovillard, 2009). (For interpretation of the references to colour in this figure legend, the reader is referred to the web version of this article.)

all, the IF samples from the Urucum region are enriched in Mo over Cr and U, and plot along a rough correlation trend in Cr_{EF} vs. Mo_{EF} space (Fig. 9a). There are two samples with low Cr_{EF} (those samples from 200 m and 100 m; Fig. 10). We however note an excessive scatter of samples from M. Grande, M. Urucum and M. Rabichão studied herein, with a tendency to exhibit slightly higher Cr_{EF} relative to Mo_{EF} compared to the other samples. The samples from M. Grande, M. Rabichão and M. Urucum studied herein are compatible

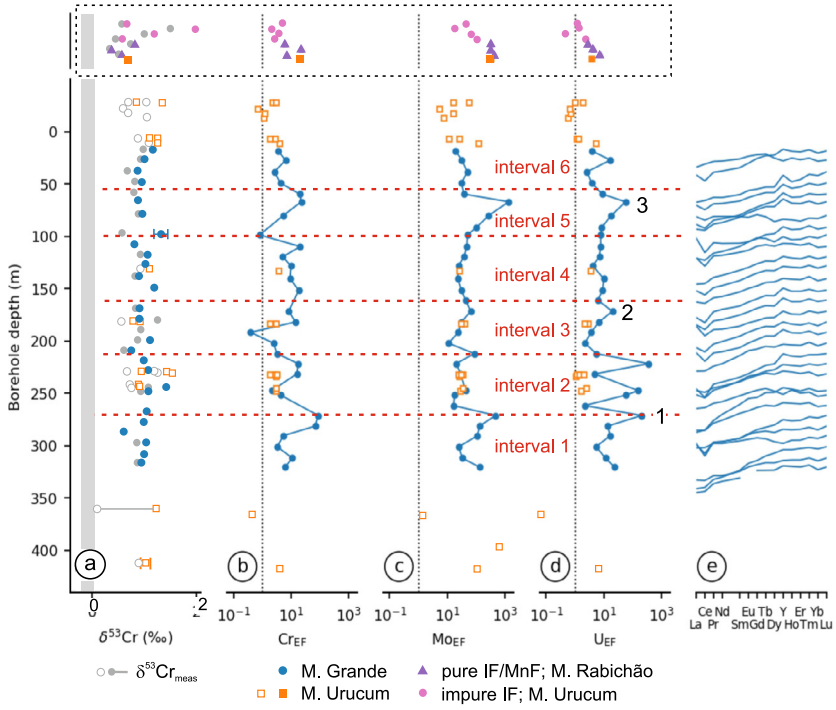

Fig. 10. Stratigraphic variation of $\delta^{53}Cr_{auth}$ values, redox sensitive element EFs and PAAS normalized REY patterns. Bore hole depths correspond to those in Fig. 5, which contains the respective units and lithologies: (a) $\delta^{53}Cr_{auth}$ blue filled circles are hematite mesoband samples from this study plotted with corresponding $\delta^{53}Cr_{meas}$ filled grey circles (b) Cr_{EF}; (c) Mo_{EF}; (d) U_{EF}; (e) Shale normalized REY patterns (Taylor and McLennan, 1985), Lu centered on sample depth. Open symbols (orange squares) indicate surface sample data from (Frei et al., 2017), plotted at approximate stratigraphic level. Samples without stratigraphic relation, analyzed for Cr isotope compositions herein, are plotted in the insert above (symbols as in Fig. 5). (For interpretation of the references to colour in this figure legend, the reader is referred to the web version of this article.)

in U_{EF} vs. Mo_{EF} space (Fig. 9b) with results from previous studies but are shifted towards slightly elevated U_{EF}. Four samples yielded particularly high U_{EF} (Fig. 9b).

Cr_{EF} show strong fluctuations, also on short depositional scales, along the drillcore profile studied (Fig. 10). The down-log Mo_{EF} and U_{EF} signals can be divided into six intervals: (1) an increasing EF trend near the base (270–330 m; 2) an interval with decoupling of Mo_{EF} and U_{EF} (270–220 m; 3) an interval with increasing and steady Mo_{EF} and U_{EF} (220–170 m; 4) an interval with relatively constant Mo_{EF} and U_{EF} (170–100 m; 5) an interval with 100 fold increase in EF (100–70 m); and (6) an interval characterized by a sharp decline to EF background values of ca. 10 (70–10 m). If those two samples with small Cr_{EF} and those 3 samples with high U_{EF} are excluded, then there is a weak correlation trend between Cr_{EF}, Mo_{EF} and U_{EF} in the hematite mesoband samples from M. Grande, M. Rabichão and M. Urucum analyzed in this study (Figs. 9, 10).

5.4. Cr-isotopes

The measured $\delta^{53}Cr_{SRM979}$ of IF mesobands are in the range from +0.5 to +1.0 ‰ (Table 1). There is no significant stratigraphic variation in the $\delta^{53}Cr$ signal (Figs. 5, 10), nor is there any significant correlation between the Cr isotope composition and Cr and major element concentrations, particularly not with Al_2O_3 and TiO_2, which discriminate against siliciclastic detrital contamination (Fig. 5). Previous studies have reported authigenic Cr isotope compositions that were calculated by correcting for detrital input (Frei et al., 2017; Gilleaudeau et al., 2016), assuming a fixed ratio between Cr and an immobile reference element in the detrital component, and assuming the complete immobility of the other element (e.g. Al, Ti, Th or Zr). Using simple mass balance for a two end-member mixture, we can correct for detrital influence with the following equations (Gilleaudeau et al., 2018):

(1) $Cr_{det\ sam} = Cr_{PAAS} * Al_2O_{3sam\ meas}/Al_2O_{3PAAS}$
(2) % $Cr_{det} = (Cr_{det\ sam}/Cr_{sam\ meas}) * 100$
(3) $\delta^{53}Cr_{auth} = (\delta^{53}Cr_{meas} - (\delta^{53}Cr_{PAAS} * (\%\ det\ Cr_{sam}/100)))/(1 - (\%\ det\ Cr_{sam}/100))$

Where the subscripts "sam", "meas", "det" and "auth", refer to sample, measured, detritally-derived and authigenic, respectively.

In previous studies, the Cr/Al ratio of shale compilations were used as first approximations for the composition of the detrital component, e.g. PAAS, 110 μg/g Cr, 18.90 % wt. Al_2O_3 (Taylor and McLennan, 1985). This however induced a clear forced regression in ln Al_2O_3 - $\delta^{53}Cr$ space, indicating a lower Cr concentration in the contaminant. An iterative least squares approach instead was employed to determine the relative Cr concentration in the detrital contaminant. The $\delta^{53}Cr_{auth}$ was repeatedly calculated for all IF samples while iteratively changing the assumed Cr concentration of the detrital component, until no correlation was observed between Al_2O_3 and $\delta^{53}Cr_{auth}$. This approach yielded 54 μg/g Cr in the detrital material, i.e., roughly 50 % lower than in PAAS. Authigenic Cr isotope compositions, detrital Cr concentrations, and detrital Cr fractions are listed in Table 1 as well. $\delta^{53}Cr_{auth}$ values were not calculated for samples with more than 35 % detrital Cr share.

In contrast to the varying trends observed in Cr, Mo and U EF, at M. Grande, the $\delta^{53}Cr$ values do not display correlated variations. The$^{53}Cr_{auth}$ values of the mesobands studied herein (excluding the two samples with excessive detrital shares; Table 1) have a rel-

Table 1
Cr isotope signatures and Cr concentrations in IF mesobands from M. Grande and M. Rabichão.

Sample	$\delta^{53}Cr_{meas}$ ‰	$2SE_{int}$	$2SE_{ext}$	Cr_{tot} μg/g	N	Al_2O_3 %	Cr_{det} μg/g	% Cr_{det}	$\delta^{53}Cr_{auth}$ ‰
UR-51-10	1.42	0.05	0.10	19.17	2	1.51	4.31	22.51	1.87
UR-51-11	0.54	0.05	0.09	19.01	2	0.65	1.86	9.77	0.61
UR-51-20	0.62	0.04	0.09	10.56	2	0.09	0.26	2.44	0.64
UR-51-26	0.41	0.04	0.09	4.08	1	0.26	0.74	18.21	0.53
UR-51-36	0.94	0.06	0.10	20.91	2	1.04	2.97	14.21	1.12
UR-62-15	0.47	0.05	0.10	2.52	1	0.06	0.17	6.80	0.51
UR-62-25	0.31	0.04	0.09	11.19	2	0.08	0.23	2.04	0.32
UR-62-38	0.69	0.04	0.09	4.24	3	0.12	0.34	8.09	0.76
VET-01	0.91	0.04	0.09	4.47	5	0.22	0.63	14.06	1.08
VET-02	0.85	0.06	0.10	5.36	2	0.14	0.40	7.46	0.93
VET-03	0.63	0.04	0.09	2.30	5	0.15	0.43	18.63	0.80
VET-04	0.77	0.05	0.10	3.01	5	0.12	0.34	11.39	0.88
VET-05	0.79	0.06	0.10	7.04	4	0.06	0.17	2.44	0.81
VET-06	0.79	0.05	0.09	3.96	2	0.03	0.09	2.16	0.81
VET-07	0.80	0.04	0.09	2.83	8	0.09	0.26	9.09	0.89
VET-09	0.50	0.05	0.10	0.57	1	0.12	0.34	60.15	1.44
VET-10	0.72	0.06	0.10	14.66	5	0.12	0.34	2.34	0.74
VET-11	0.88	0.04	0.09	3.84	1	0.13	0.37	9.67	0.99
VET-12	0.90	0.04	0.09	12.27	1	0.21	0.60	4.89	0.95
VET-13	0.78	0.05	0.09	3.24	4	0.06	0.17	5.29	0.83
VET-14	1.08	0.07	0.10	7.58	2	0.07	0.20	2.64	1.11
VET-16	0.78	0.06	0.10	1.93	2	0.04	0.11	5.92	0.84
VET-17	0.80	0.05	0.10	6.76	3	0.08	0.23	3.38	0.83
VET-18	0.87	0.03	0.09	0.41	1	0.02	0.05	12.54	1.01
VET-19	0.80	0.09	0.12	4.65	3	0.32	0.91	19.66	1.03
VET-20	0.56	0.05	0.09	2.66	2	0.14	0.40	15.04	0.68
VET-21	0.89	0.04	0.09	10.40	1	0.10	0.29	2.75	0.92
VET-22	0.97	0.07	0.10	17.59	7	0.19	0.54	3.09	1.00
VET-23	0.99	0.06	0.10	1.37	2	0.11	0.31	22.94	1.32
VET-24	0.87	0.06	0.10	6.47	3	0.26	0.74	11.48	1.00
VET-26	0.96	0.05	0.10	15.50	1	0.03	0.09	0.55	0.97
VET-27	0.90	0.04	0.09	15.94	1	0.04	0.11	0.72	0.91
VET-28	0.49	0.05	0.10	5.36	2	0.17	0.49	9.06	0.55
VET-29	0.80	0.05	0.09	6.02	2	0.31	0.89	14.71	0.96
VET-30	0.87	0.06	0.10	10.98	4	0.17	0.49	4.42	0.92
VET-31	0.80	0.06	0.10	1.83	1	0.05	0.14	7.81	0.88

atively small scatter and define an average of +0.93 ± 0.34 ‰ (2σ, n = 28). Two samples show anomalously low $\delta^{53}Cr_{auth}$ values at around +0.55 and 0.68 ‰ (Table 1; Fig. 10), but these values are not correlated with respective EF of redox sensitive elements (Fig. 10). The M. Rabichão pure IF samples from (Viehmann et al., 2016) analyzed for Cr isotopes herein yield an average $\delta^{53}Cr_{auth}$ = + 0.53 ± 0.44 ‰ (2σ, n = 3; Table 1), and the impure samples from M. Urucum (Viehmann et al., 2016) analyzed for Cr isotopes in this study are characterized by excessively scattered data with an average $\delta^{53}Cr_{auth}$ = +0.95 ± 1.12 ‰ (2σ, n = 5; Table 1) documenting the impureness and the resulting imprecision in calculating authigenic signatures of these samples.

6. Discussion

6.1. Major element observations

With reference to major elements, the bulk core samples from the Banda Alta Formation show three significantly different compositions: (1) Mg-Ca enriched carbonaticIF below 150 m; (2) Mg-Ca poor jaspilitic IF above 150 m; and (3) Al-Si rich bands near the base and intermittently throughout the section (Fig. 5).

The difference between the composition of the bulk samples and the analyzed IF mesoband samples reveals that, when possible, we were successful in separating pure hematite bands from carbonatic and cherty/jaspilitic IF sequences. Contrary to bulk core and surface samples studied by (Frei et al., 2017), the IF hematite mesoband samples studied herein contain negligible amounts of Al_2O_3, suggesting that most detrital material was circumvented by sample selection in all but two samples with elevated Al_2O_3. There is a divergence between the outcrop samples from M. Urucum (Frei et al., 2017) and IF samples studied herein from M. Grande regarding MgO + CaO, suggesting either that no carbonatic IF were sampled there or that carbonate minerals had been leached from surface samples as a result of weathering (Fig. 6). This difference is not apparent in the Fe_2O_3/SiO_2 ratio as both groups of samples plot along the same negatively sloped trend line in Fig. 7, indicating that Fe2O3 and SiO2 inventories in bulk cherty/jaspilitic IF have not been incongruently leached from the surface samples compared to drillcore hematite mesoband samples. Only 4 IF hematite mesoband samples show elevated MgO + CaO contents (Fig. 6) and these samples plot in the field towards carbonate bearing (carbonatic) IF in Fig. 7, showing the successful isolation and separation of the hematite also in the interval towards the CD Pedras Formation (Fig. 5,7).

For the IF to record the seawater Cr isotope composition, the detrital input must be minimal, since shales, on average, have a Cr content of ca. 110 ppm (e.g. PAAS, (Taylor and McLennan, 1985), i.e. an order of magnitude higher than the sample Cr concentrations. The low concentration of Al_2O_3 ($\ll$1 % wt.) and TiO_2 ($\ll$0.1 % wt.) does indicate that the detrital contribution is relatively minor to the Cr isotope signal for most samples (cf., Table 1).

6.2. Rare-earth element budget and water sources

Europium is enriched in high-T hydrothermal fluids relative to continentally derived solutes delivered to the oceans by rivers (Elderfield, 1988; Elderfield et al., 1997). Positive Eu-anomalies in seawater therefore correlate with the contribution of hydrothermally derived REE fraction, in particular, the contribution from high-temperature hydrothermal fluid (German et al., 1990). The presence of positive Eu-anomalies in Archean and Proterozoic BIFs is therefore indicative of the presence of high-temperature hydrothermal admixtures (Derry and Jacobsen, 1990).

Except for a single sample, the VET samples studied herein do not exhibit a positive Eu-anomaly, the only exception being sample VET-31 taken near the transitional base of the Banda Alta Formation. In the Cryogenian glaciogenic Rapitan IF, two explanations have been found for the similar lack of an Eu-anomaly: (1) sufficient oxygenation of the open ocean to inhibit long-distance transport of hydrothermally derived Eu(II) (Baldwin et al., 2012) or, (2) effective isolation of the basin from the open oceans (Klein and Beukes, 1993). The second explanation is in lieu with tectonic observations of the Jacadigo Group (Freitas et al., 2011; Graf et al., 1994; Urban et al., 1992). (Frei et al., 2017) however argue that this model fails to provide a source for the large quantities of Fe and Mn, and the diversity of REY patterns observed in sediments from the basin (Angerer et al., 2016; Frei et al., 2017; Graf et al., 1994; Klein and Ladeira, 2004; Viehmann et al., 2016), to explain the presence of low-T hydrothermal fluids and/or freshwater input to the surface waters (Freitas et al., 2011), and to accommodate the transition to the open shelf setting of the Corumbá Group carbonates succeeding the IFs (Gaucher et al., 2003).

Archean and Paleozoic hydrogenous chemical sediments often have positive Eu-anomalies. They are commonly used to imply ocean anoxia, as Eu^{2+} is more soluble in water than trivalent REE, allowing long distance transport from high-T vent systems. REY patterns from all three “morros” in the Urucum district lack positive Eu-anomalies (Angerer et al., 2016; Frei et al., 2017; Viehmann et al., 2016), similar to the Neoproterozoic Rapitan IF (Baldwin et al., 2012; Halverson et al., 2011), and also with resemblance to Early Cambrian IFs from the Jiertieke, Yelike, and Taaxi regions in Western China (Liang et al., 2006). These contradict a high-T fluid scenario as the source of Fe. (Frei et al., 2017) argue instead for low-T fluids as alternative REE source, as REY patterns published by (Frei et al., 2017) from M. Urucum are similar to those of modern low-T spring waters (Michard et al., 1993), and further suggest these are a possible Fe source because of their high Fe/Mn ratios (values between 6 and 30). This is also in line with the *syn*-tectonic depositional model for the Corumbá graben (Freitas et al., 2011), allowing deep water metal fertilization of the Jacadigo Basin (Walde and Hagemann, 2007). Considering the adjacency of M. Urucum deposit to M. Grande and M. Rabichão (Fig. 1), there are similarities but surprisingly also significant differences in the geochemical character of IFs from the different “morros” (Angerer et al., 2016; Frei et al., 2017; Viehmann et al., 2016). M. Grande and M. Rabichão IF drillcore samples have significantly lower concentrations of detritally derived elements (Al, Ti, Zr) and base metals (Cu, Co etc.) than M. Urucum (Frei et al., 2017). Our results from M. Grande drillcore samples agree with the differences in detritally-derived elements (base metals were not measured) of the (Viehmann et al., 2016) and (Angerer et al., 2016) studies. The reported differences in $\sum Fe_2O_3$ between M. Urucum and M. Grande in the above two studies are not reflected in our sample set due to selective sampling and analysis of iron rich mesobands instead of bulk rock powders. The measured REY patterns in samples from the present study do not agree with the patterns of M. Urucum surface profile samples analyzed in the study of (Frei et al., 2017) but are in line with those reported as pure IF by (Viehmann et al., 2016) for both M. Urucum and M. Rabichão, although showing a higher variation in $\sum$REE (Fig. 8). They are typically seawater like with a positively sloped pattern, with negative Ce/Ce^*_{PAAS} and positive Y_{PAAS} anomalies. Three REY types were defined by (Angerer et al., 2016) for the Santa Cruz deposit on M. Grande: (I) Seawater-like (II) positively sloped small negative Ce/Ce*; and (III) flat slightly MREE enriched patterns. All of these patterns are represented in our study (Fig. 10e).

Throughout the studied drillcore section, the patterns alternate between the seawater-like, negative Ce/Ce* and superchondritic Y/Ho ones, and steeper patterns with nearly absent Ce/Ce* and sup-

pressed, near-chondritic Y/Ho (Fig. 10). Three of the IF samples observed on M. Grande exhibit the same flat REY pattern as seen in the underlying Urucum Formation These are similar to the "hematite mud" pattern of (Angerer et al., 2016).

The patterns observed for IF mesoband samples from M. Grande and from M. Rabichão, and from M. Urucum studied herein, are compatible with a mixing model between a seawater source and a freshwater source for REY (Fig. 11). Surface outcrop samples from M. Urucum, and iron-rich shale samples from the Puga Formation clearly plot separately in the discrimination diagrams of Fig. 11 and necessitate special attention (see below).

6.3. Effect of weathering on REY

The hump shaped PAAS normalized patterns observed in surface samples from M. Urucum by (Frei et al., 2017), do not match the model presented above. In their review of high-grade hematite-martite ores, (Gutzmer et al., 2008) show similar hump-shaped patterns, though normalized against a iron formation protolith, for supergene enriched samples from the Maremane IF, South Africa, and for ore samples from M. Urucum. They argue for retention of LREE relative to HREE in (Al-) phosphates, which formed during supergene leaching. In a quantitative mineralogical study of altered BIFs from the Witwatersrand-Mozaan Basin (South Africa), combined with observations on leaching behavior and distribution of REEs in the BIFs, (Smith et al., 2008) reached a similar conclusion that REE-bearing phosphates have a major control of the REE budget in altered BIFs of the supergene environment in that the REE phosphates accounted for up to 31 % of the REE inventory in these BIF. Re-distribution of REE into secondary phosphates has also been observed during modern weathering (Braun et al., 1990; Nelson et al., 2003), and in an andesite paleosol associated with the Maremane IF (Wiggering and Beukes, 1990). This process leads to relative enrichment of LREE over HREE (seen as e.g., high Pr/Yb), which correlates with the Fe enrichment. In the surface profile samples from M. Urucum (Frei et al., 2017), there is a correlation between Pr/Yb and Al_2O_3 (Fig. 12a), a trend which is incompatible with detrital influence, as it reaches higher Pr/Yb than PAAS and the "local" shale from the Puga Formation (Frei et al., 2017) taken here as reference, indicating a secondary process of alteration. Conversely, Pr/Yb neither correlates with P_2O_5 nor with Fe_2O_3 in the samples of Frei et al. (2017), suggesting another process than secondary phosphate scavenging leading to the observed hump-shaped patterns recorded by the surface outcrop samples. A more recent study on supergene weathering effects on the Paleoproterozoic Caué Iron Formation in the Iron Quadrangle of Brazil by (Sampaio et al., 2018) documented LREE enrichment over HREE and depressed Y/Ho ratios in altered surface-near IF samples, which these authors preferred to interpret as a result of mobilization of HREE relative to LREE in the supergene environment, along with intense leaching of silica and secondary enrichment of Fe during chemical weathering. Uncovering the nature of these processes affecting the REY patterns of surface exposed IFs from M. Urucum necessitates further detailed investigations in the future.

6.4. Detrital contribution to REY

Possible detrital contamination by transported sediments must be considered when interpreting trace element data of chemical sediments. As (Angerer et al., 2016) report, there is a significant difference between the observed REE patterns of the Banda Alta For-

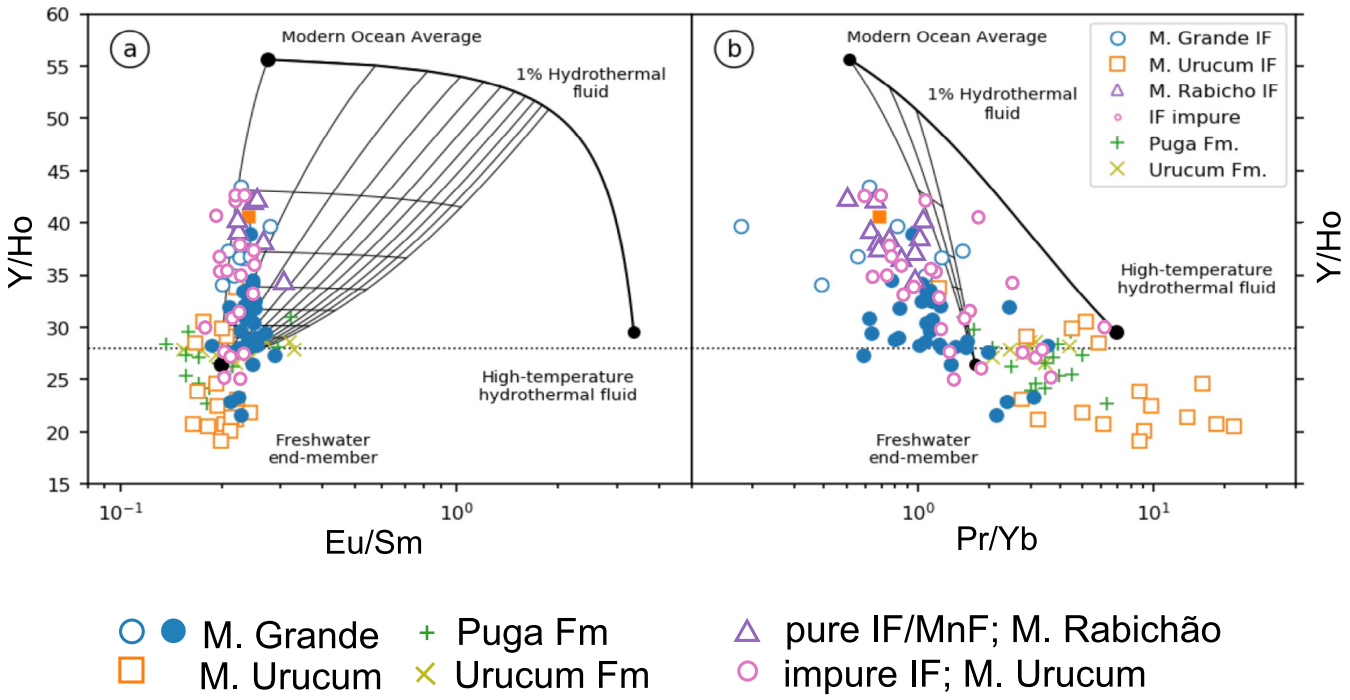

Fig. 11. Mixing model for three end-members: modern ocean average (MOA; (Alibo and Nozaki, 1999), freshwater (FW; (Lawrence et al., 2006), high-temperature hydrothermal water (HT; (Bau and Dulski, 1999). (a) Most IF samples show Y/Ho values spanning between FW and MOA. Samples from M. Urucum, in particular, display subchondritic Y/Ho. Eu/Sm ratios are compatible with FW and MOA mixtures. Gridlines are shown at 10 % intervals for FW-MOA and 0.1 % intervals between MOA and HT. (b) Apparent over dispersion in Pr/Yb, in particular for M. Urucum surface samples, and of iron-rich shales from the Puga Formation and Urucum Formation results as a consequence of supergene weathering effects and siliciclastic contamination, respectively. The bulk of pure IF samples from M. Grande and M. Rabichão however plot along a trajectory that is parallel to the FW-MOA mixing line. MOA-HT mixing lines at 0.5 and 1 %. Chondritic Y/Ho (McDonough and Sun, 1995) is indicated by the dotted line. Symbol legend as in Fig. 9. Open symbols and crosses denote data from (Angerer et al., 2016; Frei et al., 2017; Viehmann et al., 2016).

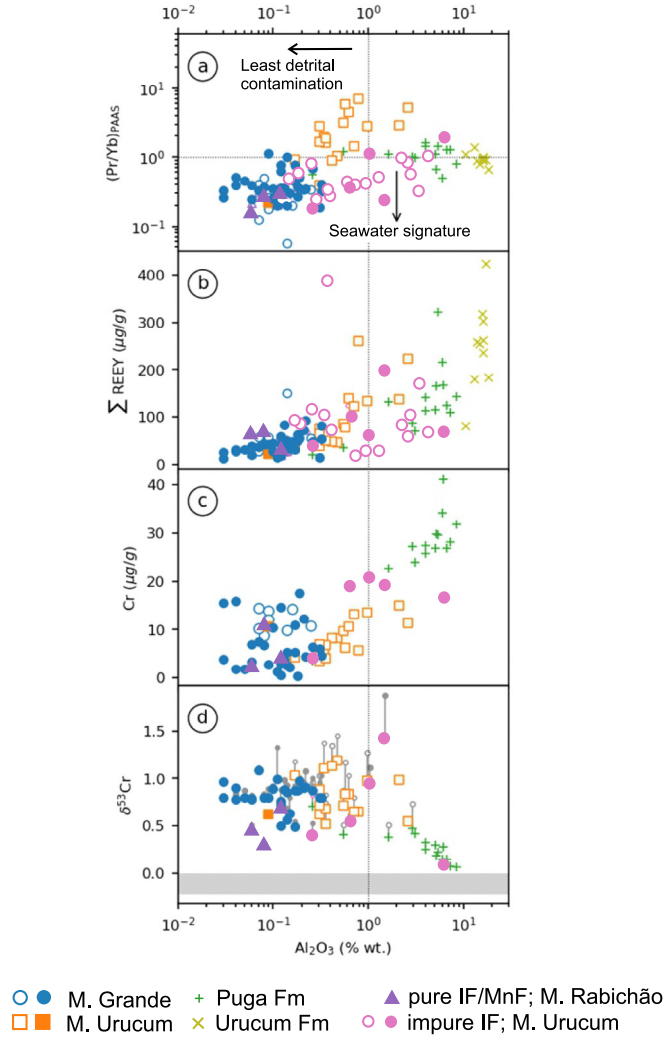

Fig. 12. Detrital influence (represented by Al_2O_3) on REY, Cr and $\delta^{53}Cr$ values in IF. (a) $(Pr/Yb)_{PAAS}$ shows no significant correlation with Al_2O_3, but there is a clear distinctive clustering of IFs from M. Grande analyzed herein (blue filled circles) from surface sample IFs at M. Urucum (empty orange squares; data from (Frei et al., 2017). This discrepancy is attributed to the effects of supergene alteration of the surface samples on the REY pattern (see text for details). (b) Correlation between total REE + Y concentration and Al_2O_3. The flat distribution depicted by the M. Grande samples studied herein (blue filled circles) in this diagram depicts that REEs are only weakly controlled by detrital siliciclastic components. (c) Lack of a systematic relationship between Cr concentration and Al_2O_3 in the IF samples from M. Grande (studied herein, blue filled circles) and in the surface IF samples from M. Urucum (empty orange squares; data from (Frei et al., 2017)) attests for a dominance of an authigenic Cr fraction in these IFs. In contrast, a significant correlation of Cr with Al_2O_3 exists in iron rich shale from the Puga Formation and in impure IFs from M. Urucum. (d) lack of correlation of raw (i.e., measured, uncorrected for Cr contribution from detrital siliciclastics) $\delta^{53}Cr$ in IF samples with below ca. 1 % wt. Al_2O_3 attests to a predominantly authigenic Cr isotope signature in these IFs. In contrast, samples from the Puga Formation show a clear trend towards unfractionated $\delta^{53}Cr$ values with rising Al_2O_3. Measured (i.e., uncorrected for contamination of Cr by detrital silicilastics) $\delta^{53}Cr$ are shown with gray open and closed circles that are connected to respective symbols marking authigenic compositions. Filled symbols are from this study. Open symbols and crosses indicate data from (Angerer et al., 2016), (Viehmann et al., 2016) and (Frei et al., 2017). The gray shaded band marks the igneous silicate Earth reservoir defined by (Schoenberg et al., 2008). (For interpretation of the references to colour in this figure legend, the reader is referred to the web version of this article.)

mation and shale composition (Fig. 8), in particular with respect to high Y_{PAAS} anomaly and pattern slope $(Pr/Yb)_{PAAS}$. However, considering the M. Grande and the M. Urucum samples studied herein and those of (Frei et al., 2017), there is a weak covariation between $(Pr/Yb)_{PAAS}$ and Al_2O_3 as well as significant covariation between ∑ REE and Al_2O_3 (Fig. 12b). Although the ∑ REE shows covariation throughout the Al concentration range, this is not reflected in the Pr/Yb ratio, which shows a distinct kink above ca. 1 wt % Al_2O_3, indicating that below this threshold detrital input is not controlling the REY budget in the iron formation.

Similar to shale normalized REY pattern of seawater (Alibo and Nozaki, 1999), the samples are characterized by depletion of LREE relative to HREE, a negative Ce/Ce* caused by sequestration of Ce^{4+} by ferromanganese crusts and nodules (Bau, 1999), as well as near-to superchondritic Y/Ho ratios (>28). The pronounced La/La* and Gd/Gd* reported for samples from M. Urucum (Viehmann et al., 2016) are not found in the M. Grande samples studied herein.

Presence of apatite as an accessory phase may significantly impact on the measured REY composition. Using a P_2O_5 average of 0.2 % wt. in the IF hematite mesobands (Table S1, range of 0.012–0.9 % wt.) as a proxy for apatite content and approximately 5000 µg/g ∑ REE in apatite (Frei et al., 2017; Nagasawa, 1970), and given the average ∑REE in the IF samples of 42 µg/g, this could account for up to ~25 % of the total REE budget for the samples (over 100 % for 0.9 % wt. P_2O_5). Although this is a significant portion of possible apatite hosted REE, no correlation is found between P_2O_5 and ∑ REE nor between P_2O_5 and MREE/HREE ratios such as represented by Pr/Yb (not shown), signals that are typical of phosphate phases (Braun et al., 1990; Nelson et al., 2003). This suggests that the potential contribution of REE from phosphates in the samples studied is not enough to alter a seawater like REY patterns to a hump-shaped one as observed in the surface IF samples from M Urucum studied by (Frei et al., 2017).

Another possible LREE and MREE contributor may be Ca-carbonates. In agreement with (Angerer et al., 2016), the lack of significant covariance of CaO with ∑REE and Pr/Yb in the IF samples, suggests that Ca-carbonates are not major contributors to the REE budget either.

6.5. Redox sensitive trace elements

Under oxic and anoxic aqueous conditions, Mo and U behave similarly. In oxic conditions they are soluble as Mo(VI) and U(VI) and display conservative behavior with long residence time, as is observed in modern seawater. Under anoxic conditions, they become particle reactive and are scavenged through adsorption to particulate matter: Fe-sulfides, Fe and Mn oxides, organic matter and clays (Algeo and Tribovillard, 2009). During deposition of iron formations, in the absence of euxinic conditions, the depositional mechanism for U(VI) and Mo(VI) is by sorption onto Fe-oxy-(hydr)oxides as particle reactive uranyl carbonate and molybdate ions. These oxides are also strong reducers for Cr in a coupled reaction, producing highly particle reactive Cr(III) which is completely stripped from the seawater (3 Fe(II) + Cr(VI) → 3 Fe(III) + Cr(III)) (Frei et al., 2009). This will naturally lead to a very short residence time for Cr. Mildly euxinic conditions are required for Mo to become particle reactive, while U is reactive without regard to presence of sulfidic species (Algeo and Tribovillard, 2009; Morford and Emerson, 1999). The relative enrichment of these elements may be used to infer redox conditions in the basin. In the open ocean with oxic bottom waters, U accumulation exceeds that of Mo, while in euxinic basins, Mo is preferentially scavenged, which would shift the basin waters to higher U/Mo ratios (Algeo and Tribovillard, 2009). Cr with a short residence time will in contrast reflect shorter time supply fluctuations.

(Frei et al., 2017) argue that in context of the observations put forward by (Algeo and Tribovillard, 2009), the Jacadigo Basin was a partially restricted basin similar to the modern Cariaco Basin off the Caribbean coast of Venezuela. Such a basin would be

bounded by a bathymetric high allowing partial mixing of basin waters with the surrounding ocean, and inhibiting mixing between surface and bottom waters (Lyons et al., 2003). The bathymetric high allows the Cariaco basin is to sustain a separate redoxcline from the open oxic ocean, allowing euxinic conditions to develop in the bottom waters, while still maintaining a steady supply of Mo from the open ocean through, e.g., a Mn/Fe shuttle. This would develop a steep Mo enriched pattern in Mo_{EF}-U_{EF} space (Fig. 9b). Should such a basin be closed off, the Mo supply would cease, and the basin would show a relative increase in U_{EF}, leading to a horizontal deviation from the partially restricted behavior caused by the silled basin in Mo_{EF}-U_{EF} space (relative U enrichment, Fig. 9b). Our data is at odds with the Jacadigo Basin being a silled basin throughout its depositional period, the intermittent relative U enrichment that is shown, in particular by 3 samples (VET-21, 23 and 24), suggests that the basin was intermittently closed off from the open ocean, allowing euxinic conditions to develop in periods where the Jacadigo Basin had limited to no exchange with oxic ocean surface water.

The relative increase in Cr_{EF}, Mo_{EF} and U_{EF} across the surface M. Urucum section observed by (Frei et al., 2017) is not as clear in the hematite mesoband samples from M. Grande studied herein. However, three separate intervals of correlated increased U-Mo content are observed (Fig. 10), and these are indicative of periods characterized by a relatively oxidized water column, allowing accumulation of U and Mo in solution. The youngest of these events is preceded by a higher abundance of siliciclastics associated with gravity flows in the drillcore indicating a period of increased seismic activity in the basin or a change in water depth (Fig. 5). There may be a causal link between these occurrences and the oxidation of the water column, as these alter the basin geometry. We note that the two Cr_{EF} depleted samples (VET-09 & 20) both have excessive detritally-derived Cr, explaining a non-authigenic Cr-isotope and Cr_{EF} signal of these samples. In accordance with the observations of (Frei et al., 2017), the samples from M. Rabichão and M. Urucum also show correlation in Cr, Mo and U EF (Figs. 9, 10).

Cr_{EF} shows larger fluctuations than Mo_{EF} and U_{EF}, which could be caused by the short residence time of Cr in a basin characterized by fast Cr removal via Fe-oxy-(hydr)oxide deposition (Fig. 10). The observed decoupling of Mo and U in the lower part of the core (250–200 m) is suggestive of ephemeral euxinic conditions during the earlier period of iron formation deposition. The existence of such conditions has been inferred by previous studies on the base of varying REY patterns (Angerer et al., 2016; Frei et al., 2017; Freitas et al., 2011).

6.6. Cr isotope signal

As suggested by (Frei et al., 2017), a constant supply of Fe(II) from anoxic waters below a redoxcline allowed efficient reductive removal of Cr(VI) from oxic surface waters, as well as removal of Mo and U. The complete removal of Cr entails that there is no significant change in Cr isotope composition during transport from surface water to the anoxic bottom waters. The reduced Cr(III) incorporated in the sediments therefore, records an authigenic surface seawater isotope signature. Cr isotopes may potentially directly record basinal input from at least four sources: (1) direct riverine input to the basin, i.e. runoff from the Rio Apa Block; (2) any subaqueous hydrothermal input to the basin; (3) input of Cr from the open ocean; and (4) via glacially sourced iron oxyhydroxides that were bacterially reduced to dissolved ferrous iron, which was subsequently oxidized to ferric iron following ice withdrawal, a model favored for the genesis of the Rapitan IF by (Baldwin et al., 2012). Model (3) would only be possible during times when there was open exchange between the Jacadigo Basin and the oceans, and it would be recorded in relative Mo enrichment over U during such time periods. Model (4) craves that during IF formational time periods, extreme primary productivity in the shallow water column drove eutrophication at middle water depths and the production of a three-tiered stratified water column with ferruginous deep water, a thin euxinic wedge at middle depths, and oxic surface water (Baldwin et al., 2012).

The short residence time of Cr, and the restricted exchange between the Jacadigo Basin and the oceans, would severely limit the effect that this connection would impact on surface water isotope composition. (Paulukat et al., 2016) have shown significant seasonal variations of the Cr isotope composition of surface water in the modern day Baltic bay, the effect of which would be exaggerated by the presence of abundant Fe(II) reductant. The lack of correlation of Cr with Mo and U supports the claim that Cr was not dominantly sourced in open ocean water, since Mo and U would have longer residence times (given absence of euxinic conditions for Mo), potentially allowing a decoupling of their abundances and their variation with Cr. This leaves us with the first two (Model 1 and 2 referred to above) plausible remaining Fe-Cr sources, namely riverine input, and subaqueous hydrothermal input that potentially could have had a control of the Cr isotopic composition of the waters of the Jacadigo Basin. The REY patterns observed at M. Grande (absence of Eu-anomalies) speak against involvement of high-T hydrothermal fluids (Model 2) in the Jacadigo Basin (Fig. 11). Rather, they indicate a mixture between a dominant fresh-water end-member, and a seawater end-member, as evidenced by the variation in slope of patterns and by the suppressed Y-Ho ratios. Low temperature hydrothermal fluids are potentially indistinguishable from fresh-water in terms of REY patterns. However, the Jacadigo Group directly overlies the high grade metamorphic rocks of the Rio Apa Block (gneisses), which are likely to be characterized by an unfractionated Cr-isotope composition, by inference with other studies which find continental rocks to be unfractionated in relation to Cr (Farkaš et al., 2013; Schoenberg et al., 2008), and by inference with the $\delta^{53}Cr$ anti-correlation with Al_2O_3 in both M. Urucum and nearby Puga Formation, which trends towards unfractionated Cr with rising Al_2O_3 (Fig. 12; (Frei et al., 2017). Additionally, during low temperature metamorphism, fluid rich systems have been shown not to impart any measurable Cr isotope fractionation (Wang et al., 2016b), suggesting that a low-T hydrothermal fluid, potentially originating from the underlying Rio Apa Block, is unlikely to introduce fractionated Cr to the Jacadigo Basin waters. Although serpentinization of peridotites has been shown to produce positively fractionated Cr in the fluid (Oze et al., 2016), to our best knowledge, the presence of peridotites in the Rio Apa Block has not been recorded, and we therefore exclude the possibility of Cr derived from the alteration of peridotites to explain the Cr isotope signature of the Urucum IF. Although a hydrothermal contribution cannot be excluded completely, this leaves riverine and glacially sourced input of Cr(VI) as the most likely source for positively fractionated Cr isotopes in the Jacadigo Basin.

The observed Cr isotope compositions agree with published $\delta^{53}Cr$ for late Neoproterozoic iron formations: Arroyo del Soldado Fe-cherts, Uruguay, $\delta^{53}Cr_{mean}$ + 1.3 ‰, ca. 0.55 Ga; Yerbal IF, Uruguay, $\delta^{53}Cr_{mean}$ + 1.5 ‰, ca. 0.57 Ga; Rapitan IF Canada, $\delta^{53}Cr_{mean}$ + 0.9 ‰, 0.7 Ga (all from Frei et al., 2009); the Namibian Chuos and Jakalsberg IF, Namibia, $\delta^{53}Cr_{mean}$ + 0.7 ‰ and + 0.8 ‰ respectively, 0.73 and 0.63 Ga (Frei et al., 2017); and BIFs in the basal Fulu Formation of the Xiajiajiang section (Nanhua Basin, South China), which are thought to have been deposited during the waning stage of the Sturtian glaciation, with average positively fractionated authigenic $\delta^{53}Cr$ values of 0.91 ‰ (summary of data in Table S3).

6.7. Preservation of the pristine Cr-isotope signal

In their study of the Archean Izermijn IF, (Albut et al., 2018) refuted previously published claims of positively fractionated Cr isotopes in surface samples of these BIFs (Crowe et al., 2013) to be pristine signals. The samples with positive δ^{53}Cr in the study of (Albut et al., 2018) showed clear surface weathering signs, such as complete dissolution of Fe-and Mn-carbonates, as well as complete oxidation of Fe and Mn, while the drillcore samples of the same BIF showed a lack of positively fractionated Cr isotope signal.

In six samples (VET-2, 4, 5, 9,13 and 14) from the M. Grande drill-core, partial leaching of carbonate was observed. For these, the $\delta^{53}Cr_{auth}$ is not statistically different from the other samples from M. Grande, M. Rabichão and M. Urucum. They also do not show significantly different normalized REY patterns from the other samples, some (VET-4, 5, and 9; Fig. 10) retain seawater-like patterns. This suggests that: (1) carbonate leaching did not affect the REY budget of the hematite bands in the Urucum ores; and (2) carbonate leaching did not affect the Cr isotope composition of the samples in the M. Urucum IFs.

The published δ^{53}Cr measured on surface and mine-shaft samples from the M. Urucum are positively fractionated with $\delta^{53}Cr_{auth.}$ Of +1.1 ± 0.4 ‰, 2σ, n = 16 (Frei et al., 2017). Those samples are visually similar to the drillcore samples from the M. Grande, but they show reduced CaO and MgO concentrations, potentially reflecting the surface leaching of carbonates. While the reported LREE enriched REY patterns of these samples are significantly different from the ones observed in this and other studies (Viehmann et al., 2016), the $\delta^{53}Cr_{auth}$ values are consistent with IF values from M. Grande, M. Rabichão, and pure IF from M. Urucum studied herein. For the sample suite as a whole, including M. Urucum outcrop samples, major element concentrations expected to change during surface weathering, e.g. Al_2O_3, P_2O_5, CaO, MgO, as well as REY ratios (e.g. Pr/Yb, Y/Ho) do not correlate with $\delta^{53}Cr_{auth}$, suggesting that the process affecting the REY patterns at M. Urucum did not affect the Cr isotope composition in the outcrop samples gathered by (Frei et al., 2017).

Percolation of river and groundwater is apparently responsible for the alteration of the Cr isotope signal observed in the Izermijn BIF surface samples (Albut et al., 2018). However, high topography of the Banda Alta Formation and the horst structures of the "morros", prevent interaction of the IF with modern river water. Percolation of meteoric water during tropical weathering apparently did not change the Cr isotope composition of the surface outcrop samples from Urucum.

Therefore, surface outcrop conditions of IF at Urucum cannot be directly compared to the carbonate leached Izermijn BIF outcrop samples, and we deem it unlikely, that the weathering processes, shown to have altered the Izermijn BIF Cr isotope compositions, have affected the Urucum IF in a similar manner.

6.8. Cr isotopes in ambient seawater

The observed $\delta^{53}Cr_{auth}$ values in Urucum IFs are in agreement with the range of modern day seawater δ^{53}Cr values of +0.13–1.5 3 ‰ (Bonnand et al., 2013; Bruggmann et al., 2019b; Farkaš et al., 2018; Goring-Harford et al., 2020; Goring-Harford et al., 2018; Janssen et al., 2020; Paulukat et al., 2016; Pereira et al., 2015; Rickli et al., 2019; Scheiderich et al., 2015). (Frei et al., 2017) proposed that this suggests a similar Cr cycle in the Late Neoproterozoic to the one that operates today.

Recently it has been shown that biogenic fractionation of Cr isotopes plays a major role in modern Cr cycling in the modern ocean (Janssen et al., 2020; Rickli et al., 2019). In addition, based on a water column study of the redox-stratified Lake Cadagno (Switzerland), considered a modern Proterozoic ocean analog, (Janssen et al., 2022) challenge assumptions from δ53Cr paleoredox applications that quantitative Cr reduction and removal limits isotope fractionation. These authors instead show that fractionation from non-quantitative Cr removal leads to sedimentary records offset from overlying waters and not reflecting high δ^{53}Cr from oxidative continental weathering. (Janssen et al., 2022) show that removal of isotopically light Cr through biogenic reduction of Cr either directly or through production of Cr reductants, e.g. Fe(II), is responsible for isotopically light Cr(III) deposited in the deep ocean, leaving an isotopically heavy dissolved Cr(VI) fraction in the surface layer.

A compilation from diverse permanently and seasonally anoxic systems (e.g., Black sea, Saanich Inlet and others), including Lake Cadagno, lead (Janssen et al., 2022) to postulate that non-quantitative Cr removal above the chemocline (in which ~20–60 % of [Cr] in the surface water commonly is reduced), enables the transport and accumulation of low δ^{53}Cr to anoxic deep waters from where it is poorly sequestered into sediments. Therefore, these authors excerpt concerns for reconstructions of surface water columns or weathering conditions from δ^{53}Cr signals from sediments deposited in these environments, as such reconstructions require accounting for fractionation during Cr removal as well as internal water columns cycling resulting in variable water column δ^{53}Cr.

If non-quantitative biogenic Cr reduction was the primary control on δ^{53}Cr in the Jacadigo Basin, it would require a complementary reservoir characterized by isotopically light(er) Cr. Organic-rich sediments, for example, are not recorded in the Banda Alta Formation. Given: (1) the efficiency of Cr reduction by the Fe(III) shuttle, and (2) the large amounts of dissolved Fe(II) required for IF deposition in the Jacadigo Basin, it is more likely that quantitative abiogenic Cr reduction was the predominant process for shuttling Cr from the surface waters to the sedimentary environment. This does not preclude bioproductivity (presence of phytoplankton) in the photic layer which may or not have driven dissolved Cr in the surface water even more positively fractionated before its scavenging and stripping by iron (oxy) hydroxides formed in the oxic surface waters during times of upwelling of Fe(II)-rich bottom waters. The Fe(III) shuttle would be fast and exhaustive, and therefore faithfully carrying Cr with surface water δ^{53}Cr to the seafloor. In such a scenario the effect of biogenic Cr cycling would be restricted to bioproductivity in the surface waters which would enhance the signal of isotopically heavy riverine Cr(VI) input, ultimately controlled by oxidative weathering processes on land. The scarcity of light Cr isotope signatures so far measured in Neoproterozoic IFs (Urucum/Mutun, Brazil; Fulu, China; Puga, Brazil; Chuos, Namibia; Rapitan, Canada; Arroyo del Soldado Group, Uruguay; Table S3), in fact the rather commonly observed strongly positively fractionated δ^{53}Cr values in these sediments (average δ^{53}Cr values of studied sections ranging from +0.29 to 1.32 ‰ (Table S3) (Frei et al., 2017; Frei et al., 2009; Frei et al., 2013; Wei et al., 2018b), attest for a more uniform and widespread shuttling mechanism of Cr from the surface waters to the sediment in Neoproterozoic depositional basins. Our data presented herein, of relatively homogenous and strongly positively fractionated δ^{53}Cr signatures of Fe mesobands from the c. 350 m-thick massive IF section at M. Grande supports a steady-state and effectively quantitative Cr-exhaustive fertilization of the Jacadigo Basin with Fe(II) relative to Cr(VI) during the entire depositional period. The relatively homogeneous, positively fractionated Cr isotope signal as observed in the studied section is unlikely to have resulted from significant non-quantitative Cr(VI) reduction and sequestration, as in this case rather heterogeneously distributed Cr isotope signals in the IFs would be expected. Based on the above, we prefer to interpret the authigenic δ^{53}Cr values measured herein from the M. Grande section as to closely reflect the average Cr isotope signature of the ambient surface water in the Jacadigo Basin.

6.9. Jacadigo Basin implications for seawater-atmosphere system

Based on a study on drillcore samples from the Santa Cruz deposit at M. Grande, (Angerer et al., 2016) argue for a *syn*-glacial model with deposition of IFs during a transgression-regression cycle. They envisage a scenario based on systematic variations in REY and δ^{57}Fe, in which the Jacadigo Basin acted as a marine sub-basin receiving REY from freshwater, pore water or low-temperature hydrothermal sources, as well from open ocean waters. The mixing of these different water sources, according to (Angerer et al., 2016), produced three different geochemically distinguishable iron formation facies. In their study on drill-core samples from M. Urucum and M. Rabichão, (Viehmann et al., 2016) found seawater-like REY patterns in pure iron formation and shale-like patterns in detritally contaminated IF samples. These contrast with the LREE-MREE enriched hump-shaped REY patterns observed by Frei et al. (2017) in surface samples from M. Urucum, which these authors interpreted to be more compatible with low temperature hydrothermal vent fluids (Michard et al., 1993).

Our results from M. Grande complement these studies, in that the seawater-like patterns and flat sloped fresh-water-like patterns presented herein, are similar to patterns reported by (Angerer et al., 2016) and (Viehmann et al., 2016). The prevalence of seawater-like patterns in the central to upper part of the drillcore (200–30 m), as well as sporadically elevated U_{EF}-Mo_{EF} in the lower part of the core, support the transgressive model presented by (Angerer et al., 2016) for the lower parts of the section (the upper regressive section is not present in the drillcore). Hump-shaped patterns, as observed at M. Urucum, were not observed in our study. Presence of seawater like patterns supports the interpretation of the Jacadigo Basin as a silled, partially restricted basin with periodical open ocean connection, as argued by previous authors to have been established during inter-glacial periods (Frei et al., 2017; Viehmann et al., 2016), allowing greater exchange with the open ocean caused by glacioeustatic sea-level rise. In this, the IFs of the Jacadigo Basin exhibit pronounced similarities with the depositional environments proposed for the Cryogenian Rapitan IFs (Baldwin et al., 2012). The role of Mn and Fe oxyhydroxides in the fixation and scavenging of Mo as molybdate ion from oxic seawater is fairly well documented (e.g., (Algeo and Tribovillard, 2009). Using redox sensitive element enrichment factors (Mo_{EF} and U_{EF}), and correlation diagrams of Mo vs. Fe_2O_3 and MnO, in which a strong relationship between these metals in an entirely oxic water column would be expected, (Baldwin et al., 2012) postulated that Mo enrichment in the Raptian IFs happened under euxinic conditions instead. The lack of any strong correlation between Mo, Fe_2O_3 and MnO (not shown here), across the full range of compositions, in the M. Grande samples studied herein, demonstrates that iron (and manganese) deposition rates were not a limiting factor in Mo enrichment, and that consequently a molybdate fixing particulate shuttle was not a predominant scavenging mechanism to explain the Mo_{EF} in the M. Grande IFs. Like in the Rapitan IFs, free H_2S was needed to drive Mo fixation instead (Baldwin et al., 2012). The postulation of a redox-stratified Jacadigo Basin with anoxic bottom waters and with periods where a connection to open ocean waters was established, is further corroborated by a comparison of Mo_{EF} vs U_{EF} behavior (Fig. 9) with modern environmental scenarios. Unlike in restricted basins, such as the Black Sea today, a high connectivity of the upper parts of the water column with the open ocean allows for constant Mo supply. In connection with a slow exchange across the redoxcline, it allows for step Mo enrichment relative to U, which is reflected by the assembly of Urucum IF (Fig. 9) data and by published data from Rapitan IFs (Baldwin et al., 2012), and which is mirrored by modern silled basins such as the Cariaco Basin off the Caribbean coast of Venezuela (Algeo and Tribovillard, 2009).

The suggested changes in sea level associated with glacial retreat are also consistent the occurrence of Mn-beds in the lower Jacadigo Basin. These were likely deposited in shallow, more oxic environments, on expanded shallow shelves during transgressive periods (Viehmann et al., 2016). Large fluctuations in Mo_{EF}-U_{EF} ratio observed in the lower part of the drillcore would also be in support of such sea-level changes, induced by glacial advance and retreat stages.

The δ^{53}Cr in the Jacadigo Basin seems to have remained unchanged throughout the deposition of the Banda Alta Formation. (Frei et al., 2017) argued that this was due to a steady increased atmospheric oxygen activity throughout the basin lifetime. Results from this study complicate this scenario as we here observe a decoupling of Cr from the other redox sensitive trace elements, particularly from U (Fig. 9). The decoupling of Cr_{EF} from U_{EF} is enhanced in samples with elevated EF of both elements. While this scatter cannot be explained by variable siliciclastic contributions (the IF mesobands studied are very pure; see above), and because an iron oxy hydroxide shuttle is not expected to discriminate between dissolved Cr(VI) and U(VI) upon reduction, we suspect differential release/desorption/reduction mechanisms, particularly of adsorbed U, from the particulate shuttle upon transport through the redoxcline. More detailed investigations are however necessary to further elaborate on this decoupling.

6.10. A depositional model of the Urucum IF

In their study of IF from the Santa Cruz depost, (Angerer et al., 2016) proposed that the Jacadigo Basin was a redox-stratified marine sub-basin, with REY coming from the open ocean and from either low-temperature hydrothermal fluids, freshwater or pore-waters. Their model is based on the occurrence of three different IF facies observed in the Santa Cruz deposit. The work of (Viehmann et al., 2016) on M. Rabichão and M. Urucum contrasts with the study of (Angerer et al., 2016), as they find no evidence for freshwater influence. Rather, they consistently find seawater-like REY patterns, which were interpreted to imply open-ocean connection during interglacial periods. They however, recognized that the flat REY patterns observed in the Mn-horizons indicated a freshwater influx, and they proposed that these were deposited in shallow marine, more oxic shelf environments. Based on the unchanged positive $\delta^{53}Cr_{auth.}$ signal throughout the IF, and based on increasing and correlated trends for Cr_{EF}, Mo_{EF} and U_{EF} at M. Urucum, (Frei et al., 2017) argued for increasing oxidative release from the continental landmass of these redox sensitive elements during glacial retreat. (Frei et al., 2017) suggested that the model proposed by (Frei et al., 2011) for carbonates in the Ediacaran Arroyo del Soldado Group in Uruguay, may appropriately describe the processes for the Jacadigo Basin, that is: (a) During glacial periods: (1) extensive sea-ice cover reduced primary productivity, particularly on continental shelves; (2) glacial shields covered the continents isolating the surface from the atmosphere; and (3) slow weathering reactions due to low temperatures and ice cover, i.e. hindering Cr(VI), U(VI) and Mo(VI) liberation from continental sources. (b) During inter glacial periods: (1) Larger ocean surface area available to photosynthetic plankton over ice-free continental shelves; (2) exposed continents allowed release of nutrients and Cr (VI), U(VI) and Mo(VI), leading to increased bioproductivity and oxygen production; and (3) the higher temperatures accelerated chemical weathering rates.

If we are to consider all the trace-element and Cr-isotope data published on the Banda Alta Formation, then we must envisage a basin with locally varying redox conditions, and most likely the existence of several sub-basins, which were at times isolated from one-another, and there existed redox-stratified water columns where the surface layer was periodically in contact with the oxic

surface water and anoxic deep water of the open ocean in a scenario similar to that proposed for the ~600 Ma Algoma-type BIFs in the Seridó Group of northeastern Brazil by (Sial et al., 2015). Upwelling of anoxic ocean deep water would have allowed a fertilization of the Jacadigo Basin with dissolved Fe^{2+} sourced in the anoxic open ocean water layer. The correlation of Cr_{EF}, Mo_{EF} and U_{EF} (and locally also non-correlation) presented here and in data from previous studies, are consistent with oxidized surface waters and changing connectivity with the open ocean. Periods characterized by non-correlation of Cr_{EF} and U_{EF} with Mo_{EF} suggest that euxinic conditions were periodically present in the M. Grande subbasin. Short-scale enhanced fluctuations of Cr concentration, relative to U and Mo, suggests short residence time and a locally short-term changing input fluctuation for Cr. Else, these heterogeneous fluctuations of Cr in the M. Grande profile studied herein, relative to U and Mo, may reflect the changes in adsorption/reductive incorporation mechanisms of these elements on/into oxy(hydr)oxides and potential respective release from those while passing through the chemocline. These variations are in favor of a marine basin with restricted connection to the open ocean, where Fe, accumulated in a deep anoxic layer, may be derived from low-temperature hydrothermal fluids (Frei et al., 2017).

The observed REY patterns agree with the information from redox sensitive trace-elements, in that seawater like patterns recorded in the IF mostly scatter around mixing trajectories between modern seawater and freshwater patterns and/or low temperature hydrothermal fluids in Eu/Sm – Pr/Yb vs. Y/Ho spaces (Fig. 11). Regardless of whether an open-marine signal was modified in the Jacadigo Basin by a more local water mass, the lack of positive Eu anomalies (Table 1) even in samples with the highest Y/Ho is compatible with signatures in the Cryogenian Rapitan IF (Baldwin et al., 2012) and constitutes firm evidence that the Neoproterozoic ocean no longer had a prominent positive Eu anomaly derived from the input of high temperature subaqueous fluids, as reported for the Archean (e.g. (Kato et al., 2006).

The occurrence of seawater-like patterns is more common in the middle to upper part of the studied section, while the flat, freshwater like patterns are more common near the base. Although they may have been altered by supergene leaching/enrichment processes, the origin of the hump-shaped patterns in surface samples of the M. Urucum IF (Frei et al., 2017) remains unsolved, as the data presented herein from drillcore samples of M. Grande fail to reproduce such patterns. The occurrence of euxinic conditions, rapidly changing REY patterns, and the occurrence of shallow water Mn-formations in the lower part of the Banda Alta Formation, and the settling into more seawater like patterns and Mo_{EF}-U_{EF} correlation in the upper part, are in concordance with deposition during a transgressive sequence as inferred by (Angerer et al., 2016). The diminished signals for euxinic conditions in M. Rabichão and M. Urucum IFs (Fig. 9), together with the larger variations observed in REY patterns (Fig. 8) from M. Grande, indicates that these were deposited in different sub-basins. Such varying conditions have been inferred and proposed by earlier geochemical studies by (Angerer et al., 2016), (Frei et al., 2017) and (Freitas et al., 2011).

In a recent paper, (Hiatt et al., 2020) propose a model for redox-controlled rhythmites in the Cerradinho Formation of the Corumbá Group, overlying the Banda Alta Formation. They argue for a sub-ice depositional model to explain annual mm-scale biochemically - micobially-mediated precipitation of rhythmites consisting of siderite, sedimentary apatite, and hematite that occur in the Cerradinho Formation: Their model goes as follows: (a) during winter, when sea-ice was at its thickest, oxygen levels were at a minimum (microaerobic to anoxic water conditions), and methanogenesis prevailed in the sediment, leading to the formation of laminated siderite; (b) in spring, when oxygen concentrations rose and a redox gradient formed at the seafloor, biogenic phosphates were able to form on the seabed during short periods of non-deposition; (c) in summer, sea ice was at minimum thickness, and intense sunlight and maximum oxygen concentration prevailed, allowing the formation of Fe-oxy(hydr)oxides from either hydrothermally derived Fe(II), and/or deposition of iron-rich sediment derived from glacial erosion of the Banda Alta Formation, forming hematite mud laminae. They argue that ice cover inhibited deposition of siliciclastic sediments, promoting a redox-driven microbial ecosystem to develop in the basin, which allowed for the formation of the rhythmite intervals. In the perspective of this model, the redox fluctuations in the Jacadigo Basin then continued beyond the stage, where massive influx of Fe(II) leading to the deposition of the Banda Alta IFs, dominated the water column, while the basin was still (partially) ice covered.

The interpretation of the Banda Alta Formation as being deposited during a transgression, is compliant with deposition during glacial melting. The constant $\delta^{53}Cr_{auth}$ throughout the section, and the overall covariation of redox sensitive element EF in the Jacadigo Basin support this. Thin sea-ice, as in the model for the Cerradinho Formation, would have allowed an oxygenated surface layer to form, but a steady supply of Fe and sediment starvation (Freitas et al., 2011) would have kept Fe-oxy (hydr) oxide formation the primary mode of deposition throughout the Banda Alta Formation.

7. Conclusions

REY systematics and redox-sensitive trace elements (U and Mo) in pure IF mesobands of the Banda Alta Formation of the Jacadigo Group indicate that the Jacadigo Basin was partially restricted, potentially due to ice sheets, allowing exchange of surface water with surface water of the open ocean and with anoxic deep ocean water. Intermittent enrichment of U_{EF} over Mo_{EF} in the M. Grande drillcore studied herein suggests that deposition of the IFs happened in changing redox environments, some of which necessitated free H_2S in their bottom waters and therefore were occasionally euxinic.

REY systematics and U_{EF} and Mo_{EF} also support the idea of a transgressive lower Banda Alta Formation as proposed by (Angerer et al., 2016). Multiple periods of progressive enrichment of U_{EF} and Mo_{EF} suggest that there were episodes of increasing oxidation in the Jacadigo Basin surface waters, followed by relapse to less oxygenated conditions.

Short scale and timely rapid fluctuations in Cr concentration and Cr_{EF} relative to Mo_{EF} and U_{EF} indicate a very short residence time for Cr in the Jacadigo Basin during IF deposition, which is in concordance with an active and effective, Fe(II)-Fe(III)-promoted oxidation–reduction mechanism for scavenging and shuttling Cr from the surface waters to the depositional environment.

REY systematics across the Jacadigo Basin are consistent with mixture between a seawater-like and freshwater-like sources. This is indicative of the major contribution of REY, and likewise Cr, from open ocean surface waters and ultimately continental run-off.

The positively fractionated Cr isotope signatures across the Urucum IF ($\delta^{53}Cr_{auth}$ at: Morraria Grande + 0.93 ± 0.34 ‰, 2σ, n = 28; Morro do Rabichão + 0.53 ± 0.34 ‰, 2σ, n = 3; and Morro do Urucum ca. + 0.95 ± 1.12, 2σ, n = 5), in a scenario of quantitative reduction by excess fertilized Fe(II) that was oxidized in the surface water, indicate a continental source of oxidized Cr. This in turn implies relatively high atmospheric O_2 levels in the late Neoproterozoic. Our results support previous findings of positively fractionated authigenic Cr isotope signature throughout the stratigraphic section in the Urucum IF.

Although the hump-like, shale-normalized REY signals from previously published surface samples from M. Urucum are charac-

teristic of supergene alteration, the lack of correlation between δ^{53}-Cr_{auth} and indicators such as Pr/Yb, Al_2O_3, P_2O_5, and the coherence of positively fractionated $\delta^{53}Cr_{auth}$ values with those from drillcore samples studied herein, suggests that supergene alteration did not affect the Cr isotope composition at M. Urucum.

The effects of modern weathering on the Cr isotope signatures of IFs, as reported from the Archean Izermijn BIF in south Africa, are not observed in IF of the Banda Alta Formation. Selected hematite bands in samples with visible signs of leaching are statistically identical in their $\delta^{53}Cr_{auth}$ values to samples without such signs, indicating that supergene carbonate leaching processes did not affect $\delta^{53}Cr_{auth}$ either.

CRediT authorship contribution statement

Trygvi Bech Árting: Formal analysis, Writing – original draft. **Paolo César Boggiani:** Writing – review & editing. **Claudio Gaucher:** Writing – review & editing. **Henrique Albuquerque Fernandes:** Writing – review & editing. **Robert Frei:** Methodology, Conceptualization, Funding acquisition, Project administration, Supervision, Writing - original draft, Writing - review & editing.

Declaration of Competing Interest

The authors declare that they have no known competing financial interests or personal relationships that could have appeared to influence the work reported in this paper.

Acknowledgments

We thank Vectorial Ltd. for access to the Santa Cruz deposit field sites and drillcore, in particular, Raphael Henson, who provided guidance in the Vectorial mine and shared his knowledge. Thanks to technicians Toby Leeper, Toni Larsen, Cristina Nora Jensen de Olsen and Martin Heckscher. We also thank our colleagues Anja Frank, Robert Klaebe, Sylvie Bruggmann, and Jesper A. Frederiksen for vivid discussions. Thanks to Fabrício A. Caxito who accompanied us in the field, and to Sebastian Viehmann, who provided powder aliquots of samples from his and coworkers work on M. Urucum and M. Rabichão. Detailed comments by an anonymous reviewer and suggestions for improvements by associate editor Franco Pirajno are greatly acknowledged. This research is financed by the Independent Research Fund Denmark (grant 11-103378 to RF), and by CNPq (Proc2014/01233-0) and FAPESP (Proc 2014/01233-0 to PCB).

Appendix A. Supplementary material

Supplementary data to this article can be found online at https://doi.org/10.1016/j.gr.2023.06.017.

References

Albut, G., Babechuk, M.G., Kleinhanns, I.C., Benger, M., Beukes, N.J., Steinhilber, B., Smith, A.J.B., Kruger, S.J., Schoenberg, R., 2018. Modern rather than Mesoarchaean oxidative weathering responsible for the heavy stable Cr isotopic signatures of the 2.95 Ga old Ijzermijn iron formation (South Africa). Geochim. Cosmochim. Acta 228, 157–189.

Albut, G., Kamber, B.S., Brüske, A., Beukes, N.J., Smith, A.J.B., Schoenberg, R., 2019. Modern weathering in outcrop samples versus ancient paleoredox information in drill core samples from a Mesoarchaean marine oxygen oasis in Pongola Supergroup, South Africa. Geochim. Cosmochim. Acta 265, 330–353.

Algeo, T.J., Maynard, J.B., 2008. Trace-metal covariation as a guide to water-mass conditions in ancient anoxic marine environments. Geosphere 4, 872–887.

Algeo, T.J., Tribovillard, N., 2009. Environmental analysis of paleoceanographic systems based on molybdenum-uranium covariation. Chem. Geol. 268, 211–225.

Alibo, D.S., Nozaki, Y., 1999. Rare earth elements in seawater: Particle association, shale-normalization, and Ce oxidation. Geochim. Cosmochim. Acta 63, 363–372.

Allen, P.A., Etienne, J.L., 2008. Sedimentary challenge to Snowball Earth. Nat. Geosci. 1, 817–825.

Almeida, F.F.M., 1965. Geologia da Serra da Bodoquena (Mato Grosso), Brasil. Bol. Divisão Geol. Mineral. 219, 1–96.

Alvarenga, C.J.S., Boggiani, P.C., Babinski, M., Dardenne, M.A., Figueiredo, M.F., Dantas, E.L., Uhlein, A., Santos, R.V., Sial, A.N., Trompette, R., 2011. Glacially influenced sedimentation of the Puga Formation, Cuiabá Group and Jacadigo Group, and associated carbonates of the Araras and Corumbá groups, Paraguay Belt, Brazil, Geological Society, London, Memoirs. Geol. Soc. Lond., 487–497

Angerer, T., Hagemann, S.G., Walde, D.H.G., Halverson, G.P., 2016. Multiple metal sources in the glaciomarine facies of the Neoporterozoic Jacadigo iron formation in the "Santa Cruz deposti", Corumbá, Brazil. Precambrian Res. 275, 369–393.

Babinski, M., Boggiani, P.C., Trindade, R.I.F., Fanning, C.M., 2013. Detrital zircon ages and geochronological constraints on the Neoproterozoic Puga diamictites and associated BIFs in the southern Paraguay Belt, Brazil. Gondwana Res. 23, 988–997.

Baldwin, G.J., Turner, E.C., Kamber, B.S., 2012. A new depositional model for glaciogenic Neoproterozoic iron formation: insights from the chemostratigraphy and basin configuration of the Rapitan iron formation. Can. J. Earth Sci. 49, 455–476.

Basta, F.F., Maurice, A.E., Fontboté, L., Favarger, P.-Y., 2011. Petrology and geochemistry of the banded iron formation (BIF) of Wadi Karim and Um Anab, Eastern Desert, Egypt: Implications for the origin of Neoproterozoic BIF. Precambrian Res. 187, 277–292.

Bau, M., 1999. Scavenging of dissolved yttrium and rare earths by precipitating iron oxyhydroxide: Experimental evidence for Ce oxidation, Y-Ho fractionation, and lanthanide tetrad effect. Geochim. Cosmochim. Acta 63, 67–77.

Bau, M., Dulski, P., 1996. Distribution of yttrium and rare-earth elements in the Penge and Kuruman iron-formations, Transvaal Supergroup, South Africa. Precambrian Res. 79, 37–55.

Bau, M., Dulski, P., 1999. Comparing yttrium and rare earths in hydrothermal fluids from the Mid-Atlantic Ridge: implications for Y and REE behaviour during near-vent mixing and for the Y/Ho ratio of Proterozoic seawater. Chem. Geol. 155, 77–90.

Bekker, A., Slack, J.F., Planavsky, N., Krapez, B., Hofmann, A., Konhauser, K.O., Rouxel, O.J., 2010. Iron Formation: The Sedimentary Product of a Complex Interplay among Mantle, Tectonic, Oceanic, and Biospheric Processes. Econ. Geol. 105, 467–508.

Bolhar, R., Kamber, B.S., Moorbath, S., Fedo, C.M., Whitehouse, M.J., 2004. Characterisation of early Archaean chemical sediments by trace element signatures. Earth Planet. Sci. Lett. 222, 43–60.

Bonnand, P., James, R.H., Parkinson, I.J., Connelly, D.P., Fairchild, I.J., 2013. The chromium isotopic composition of seawater and marine carbonates. Earth Planet. Sci. Lett. 382, 10–20.

Braun, J.J., Pagel, M., Muller, J.-P., Bilong, P., Michard, A., Guillet, B., 1990. Cerium anomalies in lateritic profiles. Geochim. Cosmochim. Acta 54, 781–795.

Breitkopf, J.H., 1988. Iron Formations Related to Mafic Volcanism and Ensialic Rifting in the Southern Margin Zone of the Damara Orogen, Namibia. Precambrian Res. 38, 111–130.

Bruggmann, S., Klaebe, R.M., Paulukat, C., Frei, R., 2019a. Heterogeneity and incorporation of chromium isotopes in recent marine molluscs (Mytilus). Geobiology 17, 417–435.

Bruggmann, S., Scholz, F., Klaebe, R.M., Canfield, D.E., Frei, R., 2019b. Chromium isotope cycling in the water column and sediments of the Peruvian continental margin. Geochim. Cosmochim. Acta 257, 224–242.

Canfield, D.E., Poulton, S.W., Knoll, A.H., Narbonne, G.M., Ross, G., Goldberg, T., Strauss, H., 2008. Ferruginous conditions dominated later Neoproterozoic deep-water chemistry. Science 321, 949–952.

Crowe, S.A., Dossing, L.N., Beukes, N.J., Bau, M., Kruger, S.J., Frei, R., Canfield, D.E., 2013. Atmospheric oxygenation three billion years ago. Nature 501, 535–538.

D'Arcy, J., Babechuk, M.G., Dossing, L.N., Gaucher, C., Frei, R., 2016. Processes controlling the chromium isotopic composition of river water: Constraints from basaltic river catchments. Geochim. Cosmochim. Acta 186, 296–315.

Derry, L.A., Jacobsen, S.B., 1990. The chemical evolution of Precambrian seawater: Evidence from REEs in banded iron formations. Geochim. Cosmochim. Acta 54, 2965–2977.

Dorr II, J.V.N., 1945. Manganese and iron deposits of Morro do Urucum, Mato Grosso, Brazil. USGS Bull. 47.

Døssing, L.N., Dideriksen, K., Stipp, S.L.S., Frei, R., 2011. Reduction of hexavalent chromium by ferrous iron: A process of chromium isotope fractionation and its relevance to natural environments. Chem. Geol. 285, 157–166.

Droser, M.L., Gehling, J.G., 2015. The advent of animals: the view from the Ediacaran. Proc. Natl. Acad. Sci. 112, 4865–4870.

Einsele, G., 2000. Sedimentary Basins. Springer, Berlin, Heidelberg.

Elderfield, H., 1988. The oceanic chemistry of the rare-earth elements. Philos. Trans. R. Soc. Lond. A 325, 105–126.

Elderfield, H., Whitfield, M., Burton, J.D., Bacon, M.P., Liss, P.S., Charnock, H., Lovelock, J.E., Liss, P.S., Whitfield, M., 1997. The oceanic chemistry of the rare-earth elements. Philos. Trans. R. Soc. Lond. Ser. A, Math. Phys. Sci. 325, 105–126.

Eriksson, P.G., Altermann, W., Nelson, D.R., Mueller, W.U., Catuneanu, O., 2004. Chapter 5 - Evolution of the Hydrosphere and Atmosphere. In: Eriksson, P.G., Altermann, W., Nelson, D.R., Mueller, W.U., Catuneanu, O. (Eds.), Developments in Precambrian Geology. Elsevier, pp. 359–511.

Farkaš, J., Chrastný, V., Novák, M., Čadkova, E., Pašava, J., Chakrabarti, R., Jacobsen, S. B., Ackerman, L., Bullen, T.D., 2013. Chromium isotope variations (δ53/52Cr) in mantle-derived sources and their weathering products: Implications for

environmental studies and the evolution of δ53/52Cr in the Earth's mantle over geologic time. Geochim. Cosmochim. Acta 123, 74–92.
Farkaš, J., Frýda, J., Paulukat, C., Hathorne, E., Matoušková, Š., Rohovec, J., Frýdová, B., Francová, M., Frei, R., 2018. Chromium isotope fractionation between modern seawater and biogenic carbonates from the Great Barrier Reef, Australia: Implications for the paleo-seawater δ53Cr reconstructions. Earth Planet. Sci. Lett. 498, 140–151.
Frei, R., Gaucher, C., Poulton, S.W., Canfield, D.E., 2009. Fluctuations in Precambrian atmospheric oxygenation recorded by chromium isotopes. Nature 461, 250–253.
Frei, R., Gaucher, C., Dossing, L.N., Sial, A.N., 2011. Chromium isotopes in carbonates - A tracer for climate change and for reconstructing the redox state of ancient seawater. Earth Planet. Sci. Lett. 312, 114–125.
Frei, R., Gaucher, C., Stolper, D., Canfield, D.E., 2013. Fluctuations in late Neoproterozoic atmospheric oxidation - Cr isotope chemostratigraphy and iron speciation of the late Ediacaran lower Arroyo del Soldado Group (Uruguay). Gondwana Res. 23, 797–811.
Frei, R., Poire, D., Frei, K.M., 2014. Weathering on land and transport of chromium to the ocean in a subtropical region (Misiones, NW Argentina): A chromium stable isotope perspective. Chem. Geol. 381, 110–124.
Frei, R., Crowe, S.A., Bau, M., Polat, A., Fowle, D.A., Dossing, L.N., 2016. Oxidative elemental cycling under the low O_2 Eoarchean atmosphere. Sci. Rep. 6, 21058.
Frei, R., Døssing, L.N., Gaucher, C., Boggiani, P.C., Frei, K.M., Bech Árting, T., Crowe, S. A., Freitas, B.T., 2017. Extensive oxidative weathering in the aftermath of a late Neoproterozoic glaciation – Evidence from trace element and chromium isotope records in the Urucum district (Jacadigo Group) and Puga iron formations (Mato Grosso do Sul, Brazil). Gondwana Res. 49, 1–20.
Frei, R., Paulukat, C., Bruggmann, S., Klaebe, R.M., 2018. A systematic look at chromium isotopes in modern shells – implications for paleo-environmental reconstructions. Biogeosciences 15, 4905–4922.
Freitas, B.T., Warren, L.V., Boggiani, P.C., De Almeida, R.P., Piacentini, T., 2011. Tectono-sedimentary evolution of the Neoproterozoic BIF-bearing Jacadigo Group. SW-Brazil. Sediment. Geol. 238, 48–70.
Freitas, B.T., Rudnitzki, I.D., Morais, L., Campos, M.D.R., Almeida, R.P., Warren, L.V., Boggiani, P.C., Caetano-Filho, S., Bedoya-Rueda, C., Babinski, M., Fairchild, T.R., Trindade, R.I.F., 2021. Cryogenian glaciostatic and eustatic fluctuations and massive Marinoan-related deposition of Fe and Mn in the Urucum District, Brazil. Geology 49, 1478–1483.
Gaucher, C., Boggiani, P.C., Sprechmann, P., Sial, A.N., Fairchild, T., 2003. Integrated correlation of the Vendian to Cambrian Arroyo del Soldado and Corumba Groups (Uruguay and Brazil): palaeogeographic, palaeoclimatic and palaeobiologic implications. Precambrian Res. 120, 241–278.
Gaucher, C., Frimmel, H.E., Germs, G.J.B., 2009. Tectonic events and palaeogeographic evoltuion of Southwestern Gondwana in the Neoproterozoic and Cambrian. In: Gaucher, C., Sial, A.N., Halverson, G.P., Frimmel, H.E. (Eds.), Neoproterozoic-Cambrian Tectonics, Global Change and Evolution: a Focus on Southwestern Gondwana. Elsevier, Amsterdam, pp. 295–316.
Gaucher, C., Sial, A.N., Frei, R., 2015. Chapter 17 - Chemostratigraphy of Neoproterozoic Banded Iron Formation (BIF): Types, Age and Origin. In: Ramkumar, M. (Ed.), Chemostratigraphy. Elsevier, Oxford, pp. 433–449.
German, C.R., Klinkhammer, G.P., Edmond, J.M., Mitra, A., Elderfield, H., 1990. Hydrothermal Scavenging of Rare-Earth Elements in the Ocean. Nature 345, 516–518.
Gilleaudeau, G.J., Frei, R., Kaufman, A.J., Kah, L.C., Azmy, K., Bartley, J.K., Chernyavskiy, P., Knoll, A.H., 2016. Oxygenation of the mid-Proterozoic atmosphere: clues from chromium isotopes in carbonates. Geochem. Perspect. Lett. 2, 178–186.
Gilleaudeau, G.J., Voegelin, A.R., Thibault, N., Moreau, J., Ullmann, C.V., Klaebe, R.M., Korte, C., Frei, R., 2018. Stable isotope records across the Cretaceous-Paleogene transition, Stevns Klint, Denmark: New insights from the chromium isotope system. Geochim. Cosmochim. Acta 235, 305–332.
Goring-Harford, H.J., Klar, J.K., Pearce, C.R., Connelly, D.P., Achterberg, E.P., James, R. H., 2018. Behaviour of chromium isotopes in the eastern sub-tropical Atlantic Oxygen Minimum Zone. Geochim. Cosmochim. Acta 236, 41–59.
Goring-Harford, H.J., Klar, J.K., Donald, H.K., Pearce, C.R., Connelly, D.P., James, R.H., 2020. Behaviour of chromium and chromium isotopes during estuarine mixing in the Beaulieu Estuary, UK. Earth Planet. Sci. Lett. 536, 116166.
Govindaraju, K., 1984. Report (1984) on Two GIT-IWG Geochemical Reference Samples: Albite from Italy, AL-I And Iron Formation Sample from Greenland, IF-G. Geostandards Newsletter 8, 63–113.
Graf, J.L., O'Connor, E.A., van Leeuwen, P., 1994. Rare earth element evidence of origin and depositional environment of Late Proterozoic ironstone beds and manganese-oxide deposits, SW Brazil and SE Bolivia. J. South. Earth Sci. 7, 115–133.
Gutzmer, J., Chisonga, B., Beukes, N., Mukhopadhyay, J., 2008. The geochemistry of banded iron formation-hosted high-grade hematite-martite iron ores. Reviews in Econ. Geol. 15, 157–183.
Halverson, G.P., Hoffman, P.F., Schrag, D.P., Maloof, A.C., Rice, A.H.N., 2005. Toward a Neoproterozoic composite carbon-isotope record. Geol. Soc. Am. Bull. 117, 1181–1207.
Halverson, G.P., Wade, B.P., Hurtgen, M.T., Barovich, K.M., 2010. Neoproterozoic chemostratigraphy. Precambrian Res. 182, 337–350.
Halverson, G.P., Poitrasson, F., Hoffman, P.F., Nédélec, A., Montel, J.-M., Kirby, J., 2011. Fe isotope and trace element geochemistry of the Neoproterozoic syn-glacial Rapitan iron formation. Earth Planet. Sci. Lett. 309, 100–112.
He, X., Chen, G., Fang, Z., Liang, W., Li, B., Tang, J., Sun, Y., Qin, L., 2020. Source identification of chromium in the sediments of the Xiaoqing River and Laizhou Bay: A chromium stable isotope perspective. Environ. Pollut. 264, 114686.
Hiatt, E.E., Pufahl, P.K., Guimarães da Silva, L., 2020. Iron and phosphorus biochemical systems and the Cryogenian-Ediacaran transition, Jacadigo basin, Brazil: Implications for the Neoproterozoic oxygenation event. Precambrian Res. 337, 105533.
Hoffman, P.F., Kaufman, A.J., Halverson, G.P., Schrag, D.P., 1998. A Neoproterozoic Snowball Earth. Science 281, 1342–1346.
Holland, H.D., 1984. The chemical evolution of the atmosphere and oceans. Princeton Univ. Press, New York.
Hsi, C.K.D., Langmuir, D., 1985. Adsorption of uranyl onto ferric oxyhydroxides - applications of the surface complexation site-binding model. Geochim. Cosmochim. Acta 49, 1931–1941.
Janssen, D.J., Rickli, J., Quay, P.D., White, A.E., Nasemann, P., Jaccard, S.L., 2020. Biological Control of Chromium Redox and Stable Isotope Composition in the Surface Ocean. Global Biogeochem. Cycles 34, e2019GB006397.
Janssen, D.J., Rickli, J., Wille, M., Sepúlveda Steiner, O., Vogel, H., Dellwig, O., Berg, J. S., Bouffard, D., Lever, M.A., Hassler, C.S., Jaccard, S.L., 2022. Chromium Cycling in Redox-Stratified Basins Challenges δ53Cr Paleoredox Proxy Applications. Geophys. Res. Lett. 49, e2022GL099154.
Johnston, D.T., Poulton, S.W., Dehler, C., Porter, S., Husson, J., Canfield, D.E., Knoll, A. H., 2010. An emerging picture of Neoproterozoic ocean chemistry: Insights from the Chuar Group, Grand Canyon, USA. Earth Planet. Sci. Lett. 290, 64–73.
Kato, Y., Yamaguchi, K.E., Ohmoto, H., 2006. Rare earth elements in Precambrian banded iron formations: Secular changes of Ce and Eu anomalies and evolution of atmospheric oxygen. In: Kesler, S.E., Ohmoto, H. (Eds.), Evolution of Early Earth's Atmosphere, Hydrosphere, and Biosphere - Constraints from Ore Deposits. Geological Society of America, p. 0.
Kirschvink, J.L., 1992. Late Proterozoic low-latitude global glaciation: The snowball Earth. In: Schopf, J.W., Klein, C. (Eds.), The Proterozoic Biosphere: A MultidisciplinAry Study. Cambridge University Press, Cambridge, pp. 51–53.
Klein, C., Beukes, N.J., 1993. Sedimentology and Geochemistry of the Glaciogenic Late Proterozoic Rapitan Iron-Formation in Canada. Econ. Geol. 88, 542–565.
Klein, C., Ladeira, E.A., 2004. Geochemistry and mineralogy of neoproterozoic banded iron-formations and some selected, siliceous manganese formations from the Urucum district, Mato Grosso do Sul, Brazil. Econ. Geol. 99, 1233–1244.
Konhauser, K.O., Lalonde, S.V., Planavsky, N.J., Pecoits, E., Lyons, T.W., Mojzsis, S.J., Rouxel, O.J., Barley, M.E., Rosiere, C., Fralick, P.W., Kump, L.R., Bekker, A., 2011. Aerobic bacterial pyrite oxidation and acid rock drainage during the Great Oxidation Event. Nature 478, 369–373.
Lawrence, M.G., Jupiter, S.D., Kamber, B.S., 2006. Aquatic geochemistry of the rare earth elements and yttrium in the Pioneer River catchment, Australia. Mar. Freshw. Res. 57, 725–736.
Le Hir, G., Donnadieu, Y., Godderis, Y., Pierrehumbert, R.T., Halverson, G.R., Macouin, M., Nedelec, A., Ramstein, G., 2009. The snowball Earth aftermath: Exploring the limits of continental weathering processes. Earth Planet. Sci. Lett. 277, 453–463.
Lechte, M.A., Wallace, M.W., Hoffmann, K.-H., 2018. Glacio-marine iron formation deposition in a c. 700 Ma glaciated margin: insights from the Chuos Formation, Namibia. Geol. Soc. Lond. Spec. Publ. 475, 9–34.
Li, C., Love, G.D., Lyons, T.W., Fike, D.A., Sessions, A.L., Chu, X.L., 2010. A stratified redox model for the Ediacaran ocean. Science 328, 80–83.
Liang, M.C., Hartman, H., Kopp, R.E., Kirschvink, J.L., Yung, Y.L., 2006. Production of hydrogen peroxide in the atmosphere of a Snowball Earth and the origin of oxygenic photosynthesis. Proc. Natl. Acad. Sci. U.S.A. 103, 18896–18899.
Liger, E., Charlet, L., Van Cappellen, P., 1999. Surface catalysis of uranium(VI) reduction by iron(II). Geochim. Cosmochim. Acta 63, 2939–2955.
Lottermoser, B.G., Ashley, P.M., 2000. Geochemistry, petrology and origin of Neoproterozoic ironstones in the eastern part of the Adelaide Geosyncline, South Australia. Precambrian Res. 101, 49–67.
Lyons, T.W., Werne, J.P., Hollander, D.J., Murray, R.W., 2003. Contrasting sulfur geochemsitry and Fe/Al and Mo/al ratios across the last oxic-to-anoxic transition in the Cariaco Basin, Venezuela. Chem. Geol. 195, 131–157.
Macdonald, F.A., Schmitz, M.D., Crowley, J.L., Roots, C.F., Jones, D.S., Maloof, A.C., Strauss, J.V., Cohen, P.A., Johnston, D.T., Schrag, D.P., 2010. Calibrating the Cryogenian. Science 327, 1241–1243.
Marx, S.K., Kamber, B.S., 2010. Trace-element systematics of sediments in the Murray-Darling Basin, Australia: sediment provenance and paleoclimate implications of fine scale heterogeneity. Appl. Geochem. 25, 1221–1237.
McDonough, W.F., Sun, S.-S., 1995. The composition of the Earth. Chem. Geol. 120, 223–253.
McLennan, S.M., 1989. Rare earth elements in sedimentary rocks; influence of provenance and sedimentary processes. Rev. Mineral. Geochem. 21, 169–200.
Michard, A., Michard, G., Stuben, D., Stoffers, P., Cheminee, J.L., Binard, N., 1993. Submarine thermal springs associated with young volcanos - The Teahitia vents, Society Islands, Pacific-Ocean. Geochim. Cosmochim. Acta 57, 4977–4986.
Morais, L., Fairchild, T.R., Lahr, D.J.G., Rudnitzki, I.D., Schopf, J.W., Garcia, A.K., Kudryavtsev, A.B., Romero, G.R., 2017. Carbonaceous and siliceous Neoproterozoic vase-shaped microfossils (Urucum Formation, Brazil) and the question of early protistan biomineralization. J. Paleontol. 91, 393–406.
Morais, L., Freitas, B.T., Fairchild, T.R., Toniolo, T.F., Campos, M.D.R., Prado, G.M.E.M., Silva, P.A.S., Rudnitzki, I.D., Lahr, D.J.G., Leme, J.M., Philippot, P., Lopez, M., Trindade, R.I.F., 2021. Diverse vase-shaped microfossils within a Cryogenian glacial setting in the Urucum Formation (Brazil). Precambrian Res. 367, 106470.

Morford, J.L., Emerson, S., 1999. The geochemistry of redox sensitive trace metals in sediments. Geochim. Cosmochim. Acta 63, 1735–1750.
Nagasawa, H., 1970. Rare Earth concentrations in zircons and apatites and their host dacites and granites. Earth Planet. Sci. Lett. 9, 359.
Narbonne, G.M., 2005. The ediacarabiota: Neoproterozoic origin of animals and their ecosystems. Ann. Rev. Earth Planet. Sci. 33, 421–442.
Nelson, B.J., Wood, S.A., Osiensky, J.L., 2003. Partitioning of REE between solution and particulate matter in natural waters: a filtration study. J. Solid State Chem. France 171, 51–56.
Novak, M., Kram, P., Sebek, O., Andronikov, A., Chrastny, V., Martinkova, E., Stepanova, M., Prechova, E., Curik, J., Veselovsky, F., Myska, O., Stedra, V., Farkas, J., 2017. Temporal changes in Cr fluxes and δ53Cr values in runoff from a small serpentinite catchment (Slavkov Forest, Czech Republic). Chem. Geol. 472, 22–30.
Nozaki, Y., Zhang, J., Amakawa, H., 1997. The fractionation between Y and Ho in the marine environment. Earth Planet. Sci. Lett. 148, 329–340.
Oyantcabal, P., Siegesmund, S., Wemmer, K., Presnyakov, S., Layer, P., 2009. Geochronological constraints on the evolution of the southern Dom Feliciano Belt (Uruguay). J. Geol. Soc. 166, 1075–1084.
Oze, C., Bird, D.K., Fendorf, S., 2007. Genesis of hexavalent chromium from natural sources in soil and groundwater. Proc. Natl. Acad. Sci. 104, 6544–6549.
Oze, C., Sleep, N.H., Coleman, R.G., Fendorf, S., 2016. Anoxic oxidation of chromium. Geology 44, 543–546.
Parry, L.A., Boggiani, P.C., Condon, D.J., Garwood, R.J., Leme, J.d.M., McIlroy, D., Brasier, M.D., Trindade, R., Campanha, G.A.C., Pacheco, M.L.A.F., Diniz, C.Q.C., Liu, A.G., 2017. Ichnological evidence for meiofaunal bilaterians from the terminal Ediacaran and earliest Cambrian of Brazil. Nat. Ecol. Evol. 1, 1455–1464.
Partin, C.A., Lalonde, S.V., Planavsky, N.J., Bekker, A., Rouxel, O.J., Lyons, T.W., Konhauser, K.O., 2013. Uranium in iron formations and the rise of atmospheric oxygen. Chem. Geol. 362, 82–90.
Paulukat, C., Dossing, L.N., Mondal, S.K., Voegelin, A.R., Frei, R., 2015. Oxidative release of chromium from Archean ultramafic rocks, its transport and environmental impact - A Cr isotope perspective on the Sukinda valley ore district (Orissa, India). Appl. Geochem. 59, 125–138.
Paulukat, C., Gilleaudeau, G.J., Chernyavskiy, P., Frei, R., 2016. The Cr-isotope signature of surface seawater - A global perspective. Chem. Geol. 444, 101–109.
Peltier, W.R., Liu, Y.G., Crowley, J.W., 2007. Snowball Earth prevention by dissolved organic carbon remineralization. Nature 450, 813–U811.
Pereira, N.S., Voegelin, A.R., Paulukat, C., Sial, A.N., Ferreira, V.P., Frei, R., 2015. Chromium-isotope signatures in scleractinian corals from the Rocas Atoll, Tropical South Atlantic. Geobiology 14, 54–67.
Piacentini, T., Boggiani, P.C., Yamamoto, J.K., Freitas, B.T., da Cruz Campanha, G.A., 2007. Formação ferrífera associada à sedimentação glaciogênica da Formação Puga (Marinoano) na Serra da Bodoquena, MS. Revista Brasileira de Geociências 37, 530–541.
Piacentini, T., Vasconcelos, P.M., Farley, K.A., 2013. Ar-40/Ar-39 constraints on the age and thermal history of the Urucum Neoproterozoic banded iron-formation, Brazil. Precambrian Res. 228, 48–62.
Planavsky, N., Bekker, A., Hoffman, A., Lyons, T.W., 2010. Enhanced primary productivity in the aftermath of the rise of atmospheric oxygen. Geochim. Cosmochim. Acta 74, A819.
Polgári, M., Biondi, J.C., Gyollai, I., Fintor, K., Szabó, M., 2021. Origin of the Urucum iron formations (Neoproterozoic, Brazil): Textural and mineralogical evidence (Mato Grosso do Sul – Brazil). Ore Geol. Rev. 139, 104456.
Poulton, S.W., Fralick, P.W., Canfield, D.E., 2010. Spatial variability in oceanic redox structure 1.8 billion years ago. Nat. Geosci. 3, 486–490.
Rickli, J., Janssen, D.J., Hassler, C., Ellwood, M.J., Jaccard, S.L., 2019. Chromium biogeochemistry and stable isotope distribution in the Southern Ocean. Geochim. Cosmochim. Acta 262, 188–206.
Rudge, J.F., Reynolds, B.C., Bourdon, B., 2009. The double spike toolbox. Chem. Geol. 265, 420–431.
Sampaio, G.M.S., Pufahl, P.K., Raye, U., Kyser, K.T., Abreu, A.T., Alkmim, A.R., Nalini, H.A., 2018. Influence of weathering and hydrothermal alteration on the REE and δ56Fe composition of iron formation, Cauê Formation, Iron Quadrangle, Brazil. Chem. Geol. 497, 27–40.
Scheiderich, K., Amini, M., Holmden, C., Francois, R., 2015. Global variability of chromium isotopes in seawater demonstrated by Pacific, Atlantic, and Arctic Ocean samples. Earth Planet. Sci. Lett. 423, 87–97.
Schoenberg, R., Zink, S., Staubwasser, M., von Blanckenburg, F., 2008. The stable Cr isotope inventory of solid Earth reservoirs determined by double spike MC-ICP-MS. Chem. Geol. 249, 294–306.
Sial, A.N., Campos, M.S., Gaucher, C., Frei, R., Ferreira, V.P., Nascimento, R.C., Pimentel, M.M., Pereira, N.S., Rodler, A., 2015. Algoma-type Neoproterozoic BIFs and related marbles in the Seridó Belt (NE Brazil): REE, C, O, Cr and Sr isotope evidence. J. South. Earth Sci. 61, 33–52.
Slack, J.F., Grenne, T., Bekker, A., Rouxel, O.J., Lindberg, P.A., 2007. Suboxic deep seawater in the late Paleoproterozoic: Evidence from hematitic chert and iron formation related to seafloor-hydrothermal sulfide deposits, central Arizona, USA. Earth Planet. Sci. Lett. 255, 243–256.
Smith, A., Gutzmer, J., Beukes, N., Reinke, C., Bau, M., 2008. Rare earth elements (REE) in banded iron formations - Link between geochemistry and mineralogy. Aust. Inst. Min. Metall. Publ. Ser., 651–658
Stern, R.J., 2020. The mesoproterozoic single-lid tectonic episode: prelude to modern plate tectonics. GSA Today 30, 4–10.
Stern, R.J., Mukherjee, S.K., Miller, N.R., Ali, K., Johnson, P.R., 2013. ~750Ma banded iron formation from the Arabian-Nubian Shield—Implications for understanding neoproterozoic tectonics, volcanism, and climate change. Precambrian Res. 239, 79–94.
Taylor, S.R., McLennan, S.M., 1985. The Continental Crust: Its Composition and Evolution. Blackwell, Oxford.
Trinquier, A., Birck, J.L., Allegre, C.J., 2008. High-precision analysis of chromium isotopes in terrestrial and meteorite samples by thermal ionization mass spectrometry. J. Anal. At. Spectrom. 23, 1565–1574.
Trompette, R., De Alvarenga, C.J.S., Walde, D., 1998. Geological evolution of the Neoproterozoic Corumba graben system (Brazil). Depositional context of the stratified Fe and Mn ores of the Jacadigo group. J. South. Earth Sci. 11, 587–597.
Urban, H., Stribrny, B., Lippolt, H.J., 1992. Iron and manganee deposits of the Urucum district, Mato-Grosse-do-Sul, Brazil. Econ. Geol. 87, 1375–1392.
Viehmann, S., Bau, M., Bühn, B., Dantas, E.L., Andrade, F.R.D., Walde, D.H.G., 2016. Geochemical characterisation of Neoproterozoic marine habitats: Evidence from trace elements and Nd isotopes in the Urucum iron and manganese formations, Brazil. Precambrian Res. 282, 74–96.
Walde, D.H.G., do Carmo, D.A., Guimaraes, E.M., Vieira, L.C., Erdtmann, B.D., Sanchez, E.A.M., Adorno, R.R., Tobias, T.C., 2015. New aspects of Neoproterozoic-Cambrian transition in the Corumba region (state of Mato Grosso do Sul, Brazil). Ann. Paleontol. 101, 213–224.
Walde, D.H.G., Hagemann, S.G., 2007. The Neoproterozoic Urucum/Mutun Fe and Mn deposits in W-Brazil/SE-Bolivia: assessment of ore deposit models. Zeitschrift Der Deutschen Gesellschaft Fur Geowissenschaften 158, 45–55.
Wang, X.L., Planavsky, N.J., Hull, P.M., Tripati, A.E., Zou, H.J., Elder, L., Henehan, M., 2016a. Chromium isotopic composition of core-top planktonic foraminifera. Geobiology 15, 51–64.
Wang, X.L., Planavsky, N.J., Reinhard, C.T., Zou, H.J., Ague, J.J., Wu, Y.B., Gill, B.C., Schwarzenbach, E.M., Peucker-Ehrenbrink, B., 2016b. Chromium isotope fractionation during subduction-related metamorphism, black shale weathering, and hydrothermal alteration. Chem. Geol. 423, 19–33.
Wei, W., Frei, R., Gilleaudeau, G.J., Li, D., Wei, G.-Y., Chen, C., Ling, H.-F., 2018a. Oxygenation variations in the atmosphere and shallow seawaters of the Yangtze Platform during the Ediacaran Period: Clues from Cr-isotope and Ce-anomaly in carbonates. Precambrian Res. 313, 78–90.
Wei, W., Frei, R., Klaebe, R., Li, D., Wei, G.-Y., Ling, H.-F., 2018b. Redox condition in the Nanhua Basin during the waning of the Sturtian glaciation: A chromium-isotope perspective. Precambrian Res. 319, 198–210.
Wiggering, H., Beukes, N.J., 1990. Petrography and Geochemistry of a 2000–2200-Ma-Old Hematitic Paleoalteration Profile on Ongeluk Basalt of the Transvaal Supergroup, Griqualand West, South-Africa. Precambrian Res. 46, 241–258.
Will, T.M., Gaucher, C., Ling, X.X., le Roux, P.J., Li, X.H., Li, Q.L., 2021. Ediacaran bimodal volcanism in the southernmost Dom Feliciano Belt, Uruguay: Implications for the evolution of SW Gondwana. Lithos 406–407, 106539.
Wu, W., Wang, X., Reinhard, C.T., Planavsky, N.J., 2017. Chromium isotope systematics in the Connecticut River. Chem. Geol. 456, 98–111.
Xu, D.R., Wang, Z.L., Chen, H.Y., Hollings, P., Jansen, N.H., Zhang, Z.C., Wu, C.J., 2014. Petrography and geochemistry of the Shilu Fe–Co–Cu ore district, South China: Implications for the origin of a Neoproterozoic BIF system. Ore Geol. Rev. 57, 322–350.
Young, G.M., 1976. Iron-Formation and Glaciogenic Rocks of Rapitan Group, Northwest Territories, Canada. Precambrian Res. 3, 137–158.
Yu, L., Chen, W., Zhang, B., Tian, L., Liu, S., Yang, D., Wang, L., 2022. The genesis of the early Neoproterozoic Shilu banded iron formations: Could it be applied to other iron ore deposits? Ore Geol. Rev. 140, 104424.